Nuclear rerouting of paracrine Fgf3 in source cells represses target genes to pattern morphogen responses

Sevi Durdu[1,2† *], Murat Iskar[1,2], Alicia Roig-Merino[1], Elisa Gallo[1,3], Ezgi Karaca[1,7†], Andreas Kunze[1], Erika Donà[1,8†], Peer Bork[1,4,5,6], Dirk Schübeler[2,9], Darren Gilmour[1,3† *]

[1.] European Molecular Biology Laboratory, 69117 Heidelberg, Germany
[2.] Friedrich Miescher Institute for Biomedical Research, 4058 Basel, Switzerland
[3.] Department of Molecular Life Sciences, University of Zürich, 8057 Zürich, Switzerland
[4.] Molecular Medicine Partnership Unit, University of Heidelberg and European Molecular Biology Laboratory, 69117 Heidelberg, Germany
[5.] Max Delbrück Centre for Molecular Medicine, 13125 Berlin, Germany
[6.] Department of Bioinformatics, Biocentre, University of Würzburg, 97074 Würzburg, Germany
[7.] Izmir Biomedicine and Genome Center, 35340 Izmir, Turkey
[8.] CNR Neuroscience Institute, 20854 Vedano al Lambro, Italy
[9.] Faculty of Science, University of Basel, Basel, Switzerland

[†] Current affiliation
* Corresponding authors
Lead contact: darren.gilmour@mls.uzh.ch

Abstract

Morphogen gradients pattern tissues by inducing dose-dependent transcriptional responses, yet cells that produce a morphogen often respond differently from their neighbors. Using the migrating zebrafish lateral line primordium as a tractable in vivo model of organogenesis, we uncover a cell autonomous role for the classical paracrine ligand Fgf3. Transcriptomic profiling and quantitative single-molecule imaging reveal an unexpected class of target genes, including the chemokine scavenger *cxcr7b*, whose expression decreases both when FGF receptor signaling is blocked and when Fgf3 is overexpressed. High-resolution live imaging shows that Fgf3 accumulates in the nucleus of ligand-producing cells while neighboring cells receive only extracellular ligand. Whole-embryo imaging reveals that this patterning feature is widespread across developing tissues. Mosaic gain-of-function, secretion-defective mutants, and nanobody-directed degradation demonstrate that the nuclear pool of Fgf3 autonomously represses related targets without impairing canonical receptor signaling. Structure-guided comparative trafficking assays suggest that nuclear targeting is a latent property shared by several paracrine FGFs. Together, these findings reveal a morphogen-intrinsic symmetry-breaking mechanism. Secreted Fgf3 activates generic target genes across the field and nuclear Fgf3 selectively silences a subset within source cells, hard-wiring differential responses between signal senders and receivers. We propose that dual secreted-nuclear functionality of FGF ligands may be a general strategy for patterning gene-expression during organogenesis.

Introduction

Multicellular development depends on the regulated expression of genes that drive the differentiation of cell groups into tissues and organs of defined form and function. Spatiotemporal regulation of this process is provided by potent secreted signals termed morphogens[1–3]. Fibroblast growth factors (FGF) are widely studied morphogens known to control differentiation during a wide variety of developmental processes, including early tissue specification, somitogenesis and proximodistal patterning of the limb[4–7]. Studies using these and other model tissues have provided important mechanistic insights into how morphogens trigger complex spatiotemporal patterns of gene expression[8–11]. At the molecular level, secreted FGF ligands typically activate tyrosine kinase receptor pathways that promote the phosphorylation of Ets transcription factors in the nucleus, to both enhance the transcription of positive pathway targets and repress the transcription of negative targets[7,12–15]. At the tissue-scale, expression patterning is thought to be primarily encoded in the graded distribution of FGF ligands and the differential dose-responses of target genes, with each being regulated at defined morphogen thresholds[11,16]. However, these mechanisms can be modulated by cell-specific features, that are less well understood, to further enhance diversification. For example, cells that are the source of morphogen gradients are exposed to highest ligand levels, yet in many contexts are less responsive to its effects on gene activation than their immediate neighbors[3,17,18]. In some contexts, this differential response may be the result of lower receptor expression in ligand producing cells, leading to reduced signaling[19]**.** However, general mechanisms that distinguish morphogen source cells from responders in differentiating tissues remain elusive.

FGF signaling is also essential for the development of the posterior zebrafish lateral line primordium (pLLP), a tractable *in vivo* model for studying dynamic tissue patterning at cellular resolution[20–22]. Here, spot-like sources of FGF ligand expression control the systematic assembly and deposition of rosette-like mechanosensory organs, termed neuromasts, by a migrating collective of epithelial cells[23–25]. The range of FGF action within the pLLP is restricted by the expression of Heparin Sulphate Proteoglycans (HSPGs) and the formation of multicellular lumina that concentrate the secreted ligand at the center of each neuromast progenitor, with the ECM protein Anosmin1 promoting the luminal accumulation of FGF ligands secreted by cells at the front of the primordium[26]. While these mechanisms help explain how FGF acts locally to promote neuromast assembly, it is unclear if and how FGF morphogens promote cell type diversification within these differentiating organs.

Here, we address the impact of FGF signaling on gene expression patterning in the pLLP using high-throughput gene expression profiling paired with subcellular analyses in vivo. We show that activation of signaling by tissue-specific upregulation of Fgf3 results in the transcriptional repression of a subset of genes that behave as bona fide positive targets of FGF receptor signaling, such as the key chemokine

receptor *cxcr7b*, a contradictory finding. Mosaic expression of Fgf3-GFP reveals that the repression of *cxcr7b* is autonomous to source cells and can be mediated by non-secreted forms of the ligand. Targeted-depletion experiments further confirm that this activity is mediated by a nuclear-localized pool of Fgf3. Besides contributing to the growing literature on molecules with proposed dual functionality[27] these data support a generic mechanism for distinguishing morphogen source and responder cells.

Results

To gain a comprehensive view of the gene regulatory targets of FGF signaling within the posterior lateral line primordium (pLLP), we increased and reduced FGF activity using two methods. First, we used the small molecule antagonist SU5402 to inhibit the kinase domain of FGF receptor 1, at a concentration known to inhibit FGF-dependent organ differentiation and target gene expression within the tissue ('Fgfr1 inhibited'). Second, we utilized an inducible FGF ligand expression system which we have previously shown can enhance FGF signaling levels in a tunable manner ('Fgf3 induced')[28,29]. Treated pLLP cells were isolated with high specificity, using fluorescence-activated cell sorting (FACS), based on cells expressing two specific fluorescent transgenic reporters: cxcr4b:nlsTomato[30] and cldnb:lyn-GFP[25] (Figure S1). Next, we established the gene expression profiles of wild-type, Fgfr1-inhibited, and Fgf3-GFP induced pLLPs in six replicates. Profiling and bioinformatic analysis revealed the comprehensive catalog of LLP-specific genes with distinct responses to FGF signaling (Figure 1A, Table S1).

Differential gene expression analysis identified genes whose expression was significantly impacted by Fgfr1 inhibition and Fgf3 induction (Table S1, Figure S2A, see Methods). Of the 446 differentially-expressed genes shared across both comparisons, 329 exhibited opposing expression-change after Fgf3 induction versus Fgfr1 inhibition, allowing straightforward classification as either positive or negative targets of FGF signaling. For example, expression levels of the Ets transcription *pea3 (etv4)*[14], a known positive target, increased with FGF induction and decreased upon Fgfr1 inhibition. By contrast, the expression of the transcription factor *lef1* decreased in response to FGF induction and increased with Fgfr1 inhibition, consistent with previous identification of *lef1* as a negative target of FGF signaling[31–33] (Figure 1B, Figure S2B). However, less expected was the identification of an additional group, comprising 117 differentially expressed genes that were repressed after both Fgfr1 inhibition and Fgf3-GFP induction, preventing us from assigning these to either positive or negative signaling target category (Figure 1B, Table S2). Among these genes, a notable one is the scavenger receptor *cxcr7b,* previously shown to generate local chemokine gradients that enable 'self-directed' migration of the pLLP[34,35]. Transcription of *cxcr7b* was significantly reduced after Fgfr1 inhibition, consistent with previous work, showing that its expression depends on FGF-signaling[33]. However, its expression was also significantly decreased after Fgf3 induction (Figure 1B-C, Figure S3A-C). This paradoxical response prompted further

investigation into the regulation of this novel class of DEGs using quantitative approaches that compared *cxcr7b* to the canonical positive target *pea3*. Single-molecule FISH (smFISH) analysis of wild-type pLLPs confirmed that while neither is normally transcribed at the tissue's leading domain, the expression of both genes increases in following regions where neuromast assembly is promoted by FGF signaling (Figure 1D-E). Consistently, Fgfr1 inhibition led to a reduction of both genes in these regions. However, while Fgf3-GFP induction significantly increased *pea3* expression (Figure 1D), the same manipulation repressed *cxcr7b* expression throughout the tissue[28,29] (Figure 1E), confirming this gene's unexpected response to changes in FGF activity. The non-conventional nature of *cxcr7b*'s response to FGF was highlighted by comparing it to the most closely related gene, the high sequence similarity paralog *cxcr7a*, which responded to FGF inhibition and induction as a canonical positive target, similarly to *pea3* (Figure S3D-G). Since both Fgfr1 inhibition and increased ligand-expression repress *cxcr7b* expression, we investigated the impact of directly activating FGF receptor signaling by driving mosaic expression of a constitutively active form of the receptor (caFgfr1a) in the pLLP. As shown in Figure 1F, ca-Fgfr1a triggered the cell autonomous activation of both *pea3* and *cxcr7b* in cells of leading domain, a region of the tissue where neither gene is normally expressed. These data support the conclusion that the transcription of *cxcr7b* is increased by Fgfr1 signaling but repressed by increasing expression of its ligand Fgf3 (Figure 1G).

If *cxcr7b* expression responds positively to Fgfr1 activation, how does Fgf3 induction lead to its downregulation? The first step towards answering this question came from comparing the expression of *cxcr7b* and *fgf3* at cellular resolution, using a combination of quantitative smFISH and BAC live reporters (Figure 2A-D, Figure S3H). This revealed that while *cxcr7b* was strongly expressed in neuromast progenitors, similarly to *pea3*, it was significantly lower in cells located at the center of these rosette-like assemblies (Figure 2A-B, Figure S4A). To more precisely identify cells expressing the Fgf3 ligand, we employed a fgf3:Fgf3-GFP line where a fluorescently tagged version of the gene recapitulates the endogenous expression pattern and complements ligand function in deficient embryos[29] . This revealed that while secreted Fgf3-GFP accumulates in extracellular luminal spaces, as previously described, expression of the gene is restricted to the central cells that lack *cxcr7b* (Figure 2C-D, Figure S4B). Similar mutually exclusive expression of *cxcr7* and Fgf3-GFP was observed in other regions of the lateral line (Figure 2A versus 2C, and Figure 2E). Despite the absence of *cxcr7b* expression at the centers of the rosettes, there was high expression of *pea3*, as revealed by smFISH, indicating that the absence of *cxcr7b* is not simply a consequence of a general reduction in FGF 'autocrine' signaling in these cells (Figure S4A, Figure 2B). Imaging of Fgf3-GFP also reveals that a significant component of it becomes localized to the nuclei of expressing cells, a finding that would be not predicted for a canonical signaling function[28,31,36] (Figure 2D, Figure 3A). This mutually exclusive pattern was also noted in other embryonic tissues, such as the developing pharyngeal arches and otic

placode, where cells showing nuclear Fgf3-GFP lack *cxcr7b* expression while juxtaposing neighboring cells are strongly positive, highlighting that the mechanism that generates this intriguing pattern could be at work in all *fgf3* expressing tissues in the embryo (Figure 3B, Figure S4C). In addition, we asked if similar mutually exclusive expression could underlie the non-conventional responses of other genes of this class, by turning our attention to the T-box transcription factor (*tbx1*) which, like *cxcr7b*, was identified by expression profiling as showing reduced expression after receptor inhibition and after Fgf3-GFP induction. smFISH analysis revealed that *tbx1* exhibited a response parallel to that of *cxcr7b* (Figure S4D-E). *Tbx1* expression was higher in cells neighboring Fgf3-GFP positive cells, while it was lower in the source cells (Figure 3C-D).

We next investigated whether this nuclear localization is a feature shared by other FGF family members. To this end, we performed multiple sequence alignments of the FGF family members, which confirmed the previously defined seven subgroups[37] (Figure 4A, Figure S5A). We then selected a representative member from each subgroup and predicted their structure[38] (Figure S5). We identified features indicative of nuclear localization signals (NLS), such as positively charged region[39] on the protein surface in an extended conformation (Figure S5B-E). Except for Fgf19, which is termed an 'endocrine FGF' due to its reduced affinity for heparan sulfate proteoglycans and its systemic hormonal activity[40,41], all analyzed FGF family members displayed putative nuclear targeting features that overlap with their heparan sulfate proteoglycan interaction surface. Next, we tagged these FGF family members with GFP to examine their cellular localization when over-expressed in early embryos (Figure 4B-C). This experiment not only confirmed the known nuclear localization of Fgf2 (bFGF)[42] and the exclusively extracellular localization of the endocrine Fgf19 but also revealed varying degrees of potential nuclear localization in other paracrine FGFs as previously reported[43,44]. Thus, in vivo misexpression experiments suggest that nuclear localization may be a more widespread latent feature among the paracrine class FGFs. FRAP analysis of the nuclear pool of Fgf3-GFP showed diffusion kinetics that are significantly slower than NLS-tagged GFP, being in a similar range to the widely studied transcription factor N-Myc, further highlighting potential interactions with nuclear components (Figure 4D).

The mutually exclusive expression of *fgf3* with a subset of its signaling target genes, combined with localization of the ligand to the nuclei of source cells, indicated that Fgf3 may regulate this class of genes through a mechanism distinct from its established extracellular signaling roles. To further investigate its mode of action, we used cell transplantation to generate additional sources of inducible Fgf3-GFP in newly forming lateral line neuromasts, using reporters that allowed transplanted donor cells to be unequivocally distinguished from host cells (Figure 5A). We quantified and compared the smFISH counts of *pea3* and *cxcr7b* RNAs in 3D segmented Fgf3-GFP source and neighboring cells after induction. Increased expression of the positive target *pea3* in neighbor cells confirmed that paracrine FGF

signaling is elevated, consistent with the previous demonstration that neuromast cells can share signals via common extracellular microlumen to ensure coordinated signaling[29]. Moreover, an equivalent increase in *pea3* mRNA level was also observed in source cells, consistent with the interpretation that these cells are just as responsive to the ligand they secrete as neighboring cells (Figure 5B). However, *cxcr7b* smFISH revealed that its expression was significantly and specifically reduced in experimentally generated Fgf3-GFP source cells, while no such repression was detectable in neighbors (Figure 5B, Figure S6). Thus, results from clonal expression experiments support Fgf3 having a dual mode of action in this in vivo context - promoting the transcription of this class of target genes in receiving cells via receptor-mediated autocrine and paracrine signaling, while repressing the expression of the same genes autonomously in morphogen source cells.

The data described above demonstrate that Fgf3 localizes to the nucleus in expressing cells and can repress specific target genes in a cell autonomous manner. To probe the causal link between these findings, we next performed experiments where we manipulated the intracellular transport route of Fgf3. High-resolution imaging reveals that full-length Fgf3-GFP localized both to the nucleus and to the secretory pathway in source cells, with the secreted pool becoming concentrated in the central microlumen[45] (Figure 6A, Figure S7A). We next biased Fgf3 transport by targeting the signal peptide that sends the ligand for secretion, which has the experimental benefit of being a discrete N-terminal tag that is cleaved from the ligand when it first enters the endoplasmic reticulum. Fusion of the Fgf3 signal peptide to GFP (secGFP) resulted in specific labeling of the secretory pathway and microlumen, with no detectable nuclear localization (Figure 6B, Figure S7B). Conversely, deleting the same signal peptide sequence from full-length Fgf3-GFP (nonsec-Fgf3-GFP) caused the ligand to localize exclusively to the nucleus with no detectable labelling of the secretory compartments or microlumina (Figure 6C, Figure S7C). This is consistent with nuclear localization acting as the default transport pathway when secretion is diminished. Unlike the full-length protein, nonsec-Fgf3-GFP proved to be deficient in extracellular FGF signaling, as evidenced by the absence of detectable increase in *pea3* mRNA in expressing neuromasts (Figure 6D). This finding rules out the possibility of the Fgf3 signaling via non-canonical secretion pathways. The nonsec-Fgf3-GFP protein, however, repressed *cxcr7b* expression (Figure 6D). Thus, experimental manipulation of blocking the ligand secretion suggests that nuclear Fgf3 can mediate repression of specific target genes in signal source cells.

Performing the complementary experiment, specifically interfering with Fgf3 nuclear localization, is complicated by the fact that the NLS, unlike the discrete signal peptide, is distributed across the 3D structure and overlaps with other features of the ligand (Figure S6). We therefore took an alternative approach to testing the requirement for Fgf3 nuclear localization for its gene regulatory function by designing experiments that could selectively deplete this pool while leaving signaling activity

intact. To this aim, we utilized a DeGradFP approach, where the binding anti-GFP nanobodies fused to ubiquitin ligases leads to high-specificity destruction of GFP-tagged proteins (Figure 6E, Figure S8). More specifically, we exploited previous work showing that nanobody-mediated recruitment of a particular ubiquitin ligase SPOP (AbSPOP) leads to selective degradation of GFP-tagged proteins in the nucleus without affecting cytosolic protein levels[46]. Indeed, expressing AbSPOP in the pLLP depleted Fgf3-GFP signal in the nucleus of neuromast cells while leaving the secreted luminal pool unaffected (Figure 6F). We further validated the specificity of this approach by confirming that a mutant version nanobody (mutAbSPOP), which retains functional SPOP but lacks the ability to bind GFP-tagged targets, had no effect on nuclear Fgf3-GFP levels (Figure 6G). Expression of either AbSPOP or mutAbSPOP had no detectable impact on the upregulation of *pea3* by Fgf3 induction, consistent with strong luminal fluorescence in these neuromasts, confirming that the nanobody did not impair Fgf3-GFP extracellular signaling (Figure 6H). By contrast, the selective depletion of nuclear Fgf3-GFP by AbSPOP counter-acted *cxcr7b* repression (Figure 6H). Nuclear localization of Fgf3 therefore proved to repress *cxcr7b* transcription. Thus, manipulations that specifically alter the intracellular transport and stability of Fgf3 reveal its ability to repress the expression of specific target genes in source cells through a mechanism that is decoupled from its function in extracellular signaling (Figure 6I).

Discussion

Previous studies on cell signaling have primarily focused on how gene expression patterns are shaped by secreted ligands via paracrine and autocrine signaling[3,36]. By combining live imaging of the Fgf3 ligand with gene expression profiling of its downstream targets, we have uncovered an underexplored role for this classical paracrine signal in regulating gene expression within a multicellular tissue context. We propose a patterning model in which extracellular FGF regulates the expression of canonical target genes in all signal-receiving cells, while nuclear FGF selectively represses a subset of these targets in cells that are the source of the ligand (Figure 6I). By innately distinguishing source cells from neighbors, this offers a potentially general mechanism for establishing self-organized gene expression differences across diverse tissues, such as the ear[47], pharynx[47,48]. The dual function of FGF signaling revealed here appears to introduce an additional layer of regulatory function in developmental signaling.

A major challenge of this study was experimentally deconvolving Fgf3's roles in nucleus and extracellular signaling within source cells. One way this was achieved was by interfering with its choice of protein targeting pathway. Fgf3 secretion was specifically prevented by deleting its defined N-terminal signal peptide, as confirmed by the absence of detectable signal in extracellular microlumina. This non-secreted variant localized to the nucleus and repressed *cxcr7b* transcription, consistent with

the conclusion that the nuclear localized pool does not enter the secretory pathway. Interestingly, the non-secreted variant appears less effective at suppressing *cxcr7b* transcription compared to the full-length Fgf3-GFP (Figure 6D), raising the possibility that the signal sequence, which is normally cleaved from the secreted ligand only upon translocation into the ER, may enhance the activity of the nuclear-localized form. The converse rerouting experiment - preventing nuclear targeting and promoting secretion - was not feasible due to the NLS being distributed within the protein and overlapping with other functional properties. An alternative approach, which involved attaching a nuclear export sequence to Fgf3-GFP, reduced nuclear localization as hoped but also hindered this variant from entering the secretory pathway, complicating interpretation (Figure S7D). Nevertheless, we were able to address the requirement for the nuclear pool specifically using targeted protein degradation, which abrogated Fgf3's ability to suppress *cxcr7* expression without affected its normal paracrine signaling function. Looking ahead, it will be interesting to determine whether the targeting of Fgf3 to nuclear or secretory pathways can be regulated by the embryo to provide an additional layer of adaptive control. Although beyond the scope of this initial study, further research profiling FGFs' interactions with chromatin interactions and other nuclear proteins will lead to a better understanding of how nuclear-localized FGFs exert their gene-regulatory effects on the transcription of specific genes.

The localization and cell autonomous impact of Fgf3-GFP, both at physiological expression levels and upon targeted misexpression, encouraged us to investigate the cell autonomous roles for other FGF family members. Misexpression of additional family members in early embryos indicates that nuclear functions may be a widespread feature of FGF ligands. And while it was not possible to assay the signaling activity of these six fusion proteins to the same extent as Fgf3-GFP, the observed patterns of nuclear localization in vivo were consistent with our structural predictions, FGFs with predicted NLS domains showed nuclear localization in vivo whereas those without did not. Future studies, leveraging endogenous detection of these FGF proteins will whether the observed nuclear localization occurs under normal physiological conditions or in different cellular contexts.

Together, these observed features highlight an intriguing and underexplored dimension of FGF function in development, that could also have implications for disease. The detection of nuclear-localized FGF ligands prompts a re-evaluation of the roles and subcellular localization of other signaling molecules, particularly those containing exposed positively charged regions that could promote nuclear localization, a sequence feature shared by many ECM-associated growth factors and signaling molecules[49]. Revisiting genetic disorders linked to mutations in such molecules may offer new insights[50], especially considering the potential cell autonomous activities distinct from their conventional paracrine functions[51].

Data availability

Datasets generated in this study were deposited at Gene Expression Omnibus (GEO, https://www.ncbi.nlm.nih.gov/geo/) under accession no GSE207538.

Contributions

S.D. and D.G. designed the study. S.D. performed all experiments, assisted by A.R.M for colorimetric in situ hybridizations. M.I. and S.D. analyzed the data and assembled the figures with input from P.B. and D.S.. E.G. developed the inducible ca-Fgfr1 system. A.K. generated GFP-tagged FGF ligand plasmids and assisted with 3D organ segmentation. E.K. performed FGF protein sequence and structure comparisons. E.D. cloned *cxcr7a* cDNA. S.D. and D.G. interpreted the data and wrote the paper with input from all authors.

Competing interests

The authors declare no competing financial interests.

Acknowledgements

We acknowledge Gilmour laboratory members for discussions on the manuscript. We thank Andrea Gruia, Celine Revenu, Ulrike Schulze, E.D., A.K. and M.I. for help with preprocessing embryos. We thank EMBL core facilities, Vladimir Benes and Jelena Pistolic (Genecore), Alex Perez Gonzalez (FACS), Yury Belyaev, Kota Miura, Stefan Terjung (ALMF). We thank Andrea Gruia (EMBL) and Cornelia Henkel (MLS-UZH) for fish care. S.D. acknowledges EMBO Long-Term fellowship-ALTF 1101 and Christiane-Nüsslein-Volhard stipend. D.S. acknowledges EU Horizon 2020 ERC Advanced Grant (DNAccess 884664) and support from the Novartis Research Foundation. D.G. acknowledges SNSF Grant 31003A_176235 and support from University of Zürich. E.K. acknowledges support from Izmir Biomedicine and Genome Center. E.D. acknowledges support from CNR Neuroscience Institute.

Figures

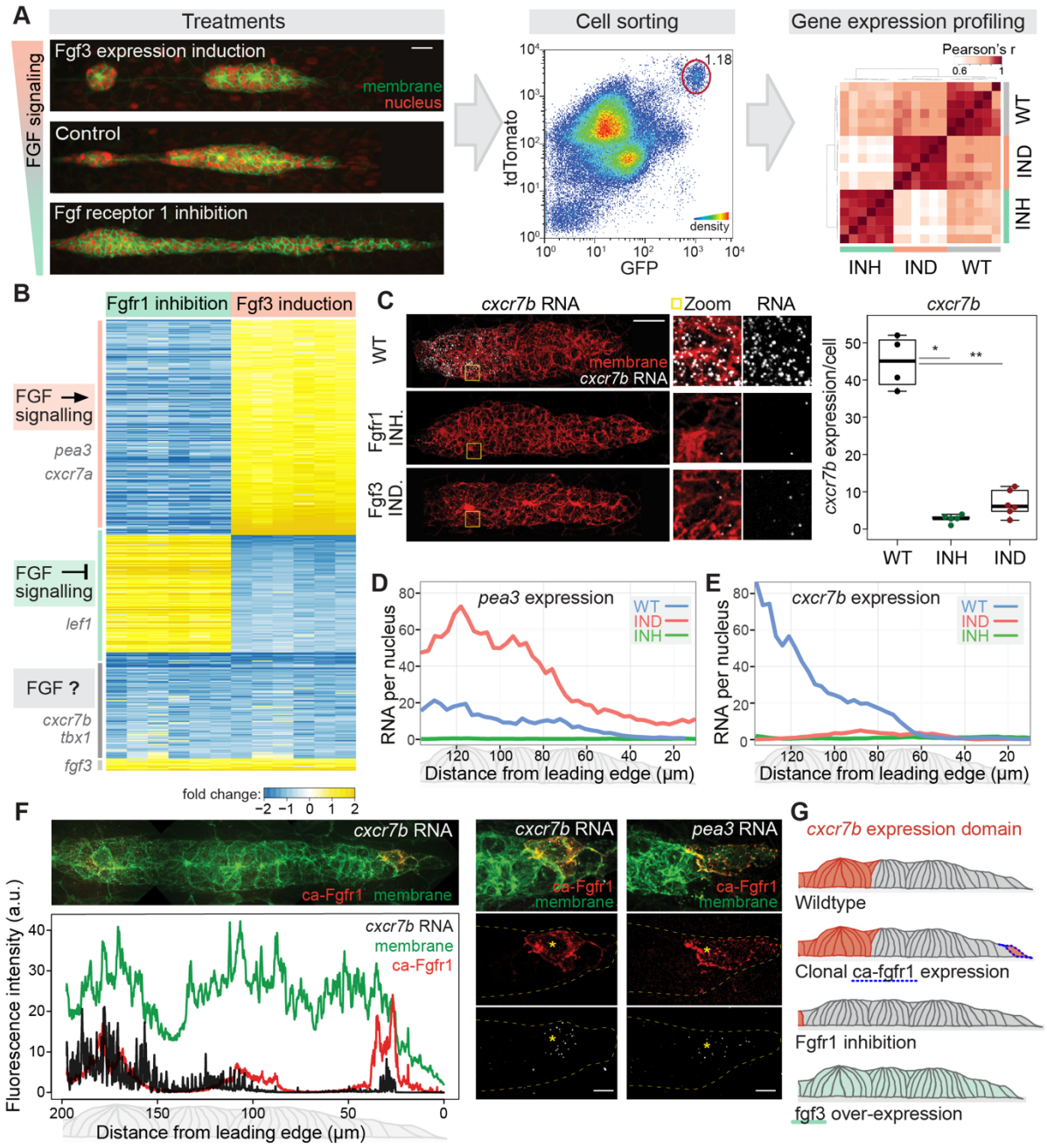

Figure 1. Gene expression profiling following FGF signaling perturbations uncovers atypical regulation of a subset of target genes in the zebrafish lateral line.

A. Gene expression profiling pipeline. Left: Images of lateral line primordium upon manipulation of FGF signaling levels through FGF ligand induction (*fgf3* over-expression) and FGF receptor inhibition (Fgfr1 kinase domain inhibition with SU5402) on cldnb:lyn-GFP (green membrane), cxcr4b:nlsTomato (red nucleus) transgenic lines together with controls. Middle: Isolation of lateral line cells from the rest of the embryo by FACS using fluorescent markers and scatter features. Red circle indicates the LLP population (See Figure S1). Right: Gene expression profiling of 6 biological replicates with 3 treatment conditions, the graph shows hierarchical

clustering of the 18 samples. **B.** Heatmap of differentially expressed genes in response to both Fgfr1 inhibition and Fgf3 induction (blue: down-regulation, yellow: up-regulation). Left: Anti-correlated genes are the dose-responsive genes oppositely affected by Fgf3 induction and Fgfr1 inhibition (e.g., *pea3* and *lef1*), and correlated genes (dose-independent) genes respond in the same direction (e.g. *cxcr7b*). Gene expression profiles recapitulate the previously documented gene expression responses to FGF signaling inhibition. Examples include *pea3* as a positive and *lef1* as a negative target of FGF signaling. **C.** smFISH based gene expression quantification of *cxcr7b* gene in LLP across wild-type (WT), FGF induction (IND) and Fgfr1 inhibition (INH) conditions. Zoomed regions are boxed. Boxplot shows cxcr7b transcript counts per cell, per primordium (n = 4, 5, 6). **D-E.** smFISH based gene expression profiles of well-characterized FGF signaling target *pea3* and the example dose-independent gene target *cxcr7b* along the LLP in wild-type, FGF induction and Fgfr1 inhibition. **F.** Probing gene expression upon clonal expression of constitutively active Fgfr1 (red, lexop:ca-fgfr1-RFP). Left panel shows the composite image of LLP with ca-Fgfr1 expressing clones and *cxcr7b* RNA smFISH on membrane labeled LLP. Plot below displays the corresponding signal intensity profiles along the migration axis. Right panel shows the activation of *pea3* and *cxcr7b* expression (white, smFISH) through clonally expressed ca-Fgfr1 (red, lexop:ca-fgfr1-RFP) at the leading edge of LLP (green, cldnb:lyn-gfp). **G.** Illustration of *cxcr7b* expression domain (red cells) upon FGF perturbations (blue lined cells: ca-fgfr1 clones, green cells: *fgf3* over-expression). Scale bars: (A, C) 20 μm, (F) 5 μm.

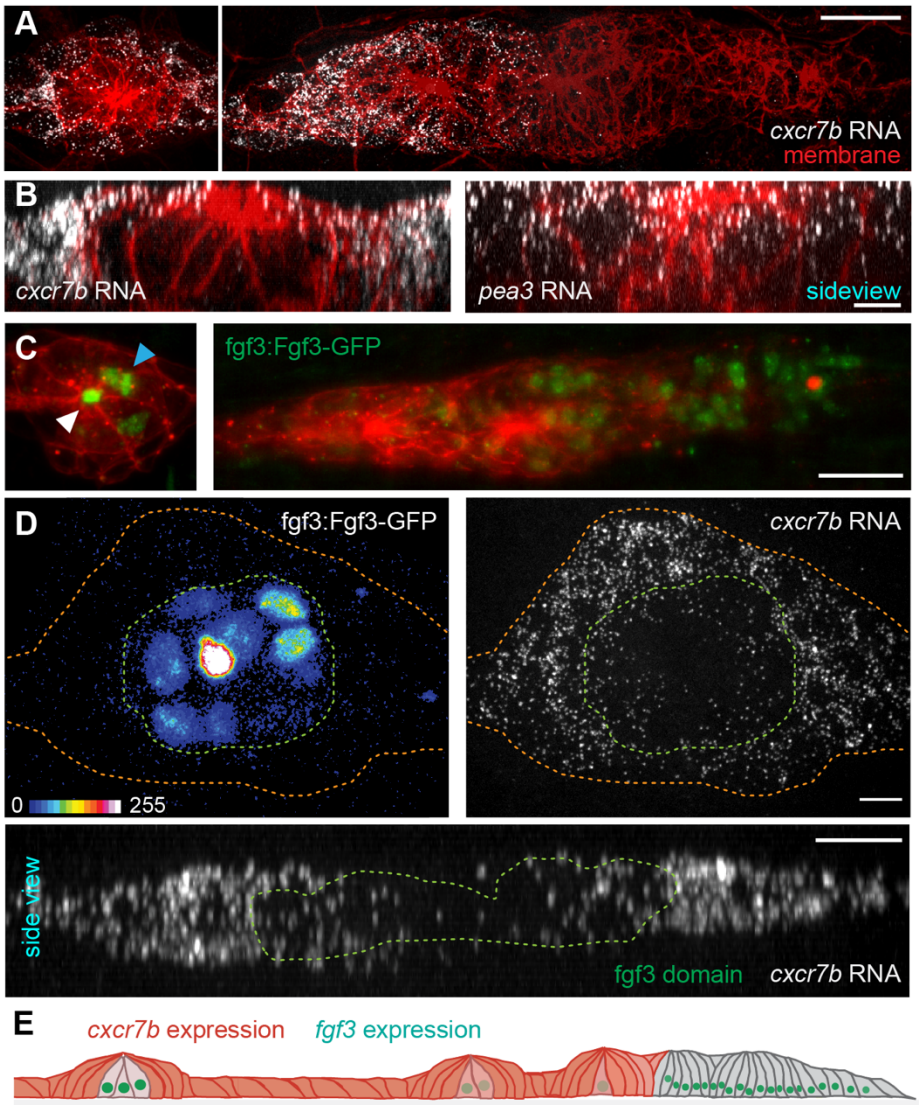

Figure 2. *fgf3* and *cxcr7b* have mutually exclusive expression patterns in the lateral line.

A. Maximal projection image of *cxcr7b* RNA smFISH (white) in lateral line (left panel: deposited organ progenitor, right panel: primordium). **B.** Side view image (middle slice) of *cxcr7b* and *pea3* RNA (white) in deposited organ progenitor (cldnb:lyn-GFP, red), to display the expression in central cells contrasting with the neighboring cells (See Figure S4A for top view). **C.** fgf3:Fgf3-GFP expression and localization in the lateral line (left panel: deposited organ progenitor, right panel: primordium). Blue arrow points to extracellular (luminal) Fgf3 and white arrow points to intracellular Fgf3. **D.** Mapping Fgf3 expression domain (green lines) versus *cxcr7b* expression domain in the same deposited organ (red lines) using fgf3:Fgf3-GFP rescue in Fgf3/Fgf10 knock-down embryos, showing centrally positioned FGF source cells with Fgf3-GFP (displayed in 16 color look-up-table), and *cxcr7b* RNA smFISH (white). Top panels show maximal projected images and bottom panel shows side view, highlighting the lack of *cxcr7b* expression in FGF source cells. (Also see Figure S4B). **E.** Illustration of observed *cxcr7b* (red) and *fgf3* (green) expression domains in lateral line (grey). Scale bars: (A and C) 20 μm, (B and D) 5 μm.

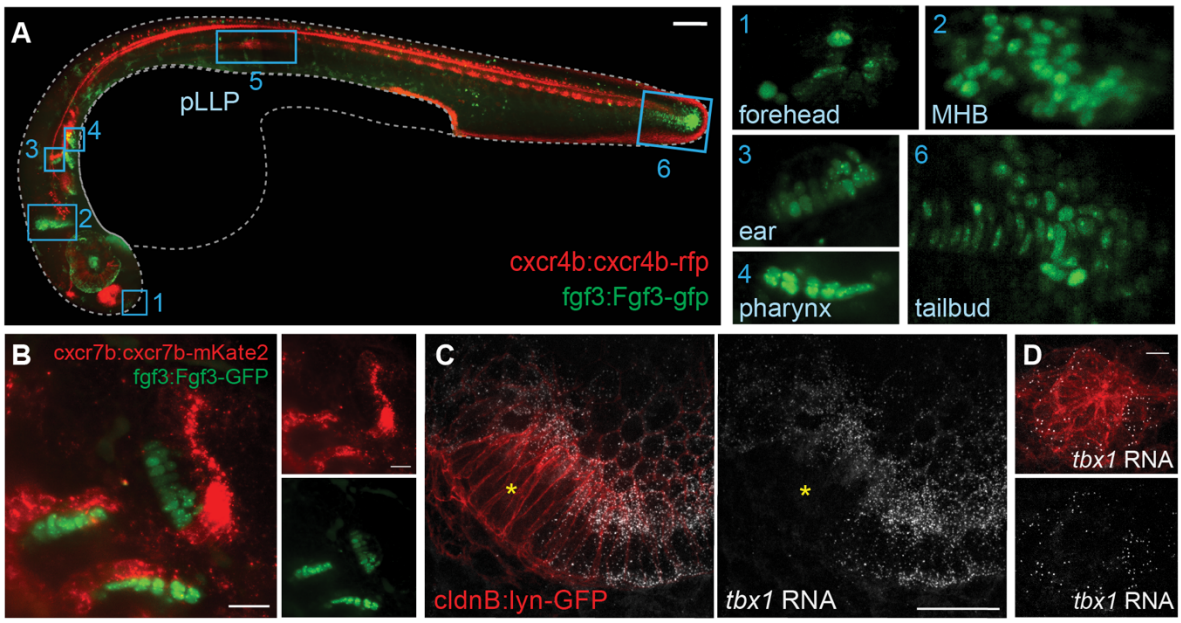

Figure 3. Fgf3-GFP shows nuclear localization and a mutually exclusive pattern with cxcr7b expression in multiple embryonic tissues.
A. fgf3:Fgf3-GFP 30 hpf zebrafish transgenic line (green) with cxcr4b:cxcrb4-RFP counter-label (red), to label anatomical regions. Known *fgf3* expression domains are revealed by the nuclear localization of Fgf3-GFP in expressing cells. Right panels show the close-up images of the boxed regions (for box #5, see pLLP in Figure 2C). **B.** fgf3:Fgf3-GFP (green), cxcr7b:cxcr7b-mKate2 (red) double transgenic fish showing mutually exclusive neighboring patterns at the developing ear and pharynx (also see Figure S4C). **C, D.** *tbx1* RNA smFISH (white) with cldnb:lyn-GFP membrane label (red) in the developing ear and a deposited organ progenitor of lateral line (also see Figure S4D). *Tbx1* gene expression is detected surrounding FGF expressing regions (described for ear in Figure 3B and for lateral line in Figure 2) but shows a contrasting pattern with the Fgf3 expressing cells (region highlighted with a yellow star). Scale bars: (A) 100 µm, (B, C) 20 µm, (D) 5 µm.

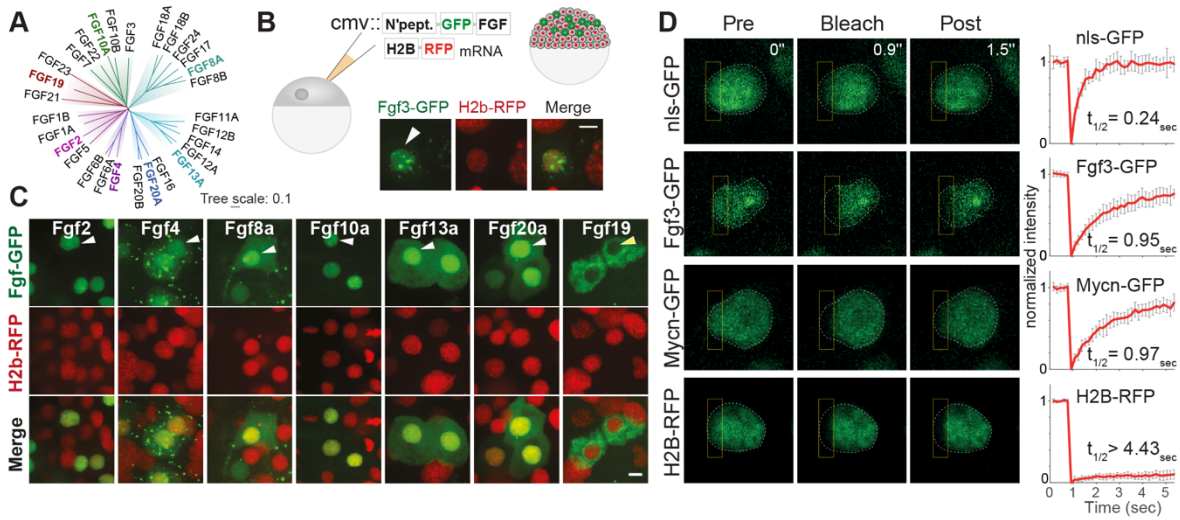

Figure 4. The nuclear localization of Fgf3 has the potential to be a widespread feature among FGFs.

A. Unrooted phylogenetic tree of FGF family members. Representative members (bold, colored) of each sub-family are chosen for further structural modelling and cellular localization experiments. **B.** Scheme summarizes the tagging and misexpression of FGF family members: transient misexpression of cmv:fgf-gfp DNA and nuclear counter-label h2b-RFP RNA (red) in 4hpf embryos. The image shows the nuclear localization of Fgf3-GFP under conditions of high, transient expression in early embryos. **C.** Cellular localization of GFP-tagged FGF family members (green) with h2b-RFP nuclear marker (red). Arrowheads (white: positive, yellow: negative) indicate nuclear localization of FGFs **D.** Comparison of Fgf3-GFP diffusion as probed with fluorescence recovery after photobleaching (FRAP), shows slower diffusion than GFP-tagged with nuclear localization signal and comparable diffusion to the transcription factor Mycn-GFP. The images show pre- and post-bleach time-points of nls-GFP, Fgf3-GFP, Mycn-GFP (transcription factor) and H2b-RFP (histone). The bleached area is marked with a rectangle. Plots show the recovery after bleaching of 10 replicates. H2b-RFP did not reach recovery within the imaged duration, as expected. Calculated mobile fraction: 0.98, 0.83, 0.86, $t_{1/2}$: 0.24, 0.95, 0.97, respectively. Scale bars: (B-C) 10 µm.

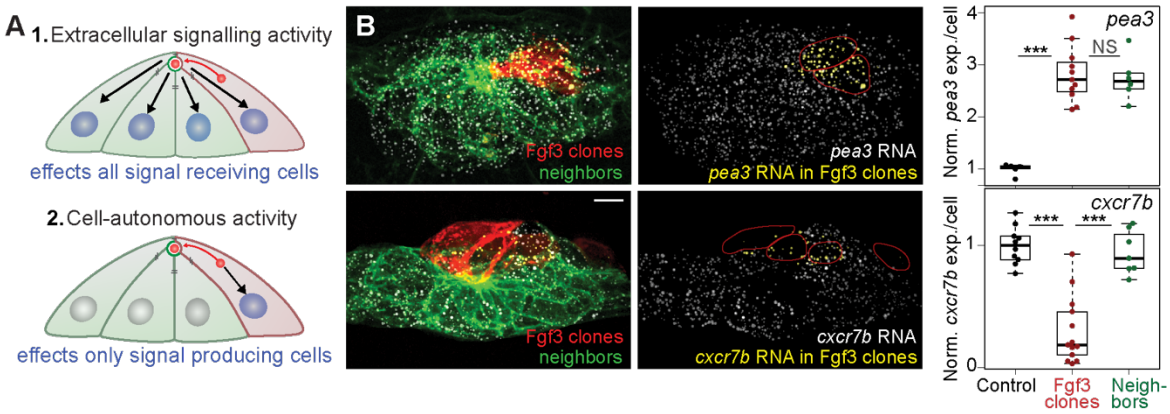

Figure 5. Clonal misexpression of Fgf3 leads to increased signaling in all organ progenitor cells but cell autonomous down-regulation of *cxcr7b* expression specifically in source cells.
A. Schema showing possible outcomes of ectopically expressing Fgf3 in clones. Fgf3 misexpressing cells are drawn in red, all other cells in the same organ progenitor (neighbors) are drawn in green. **B.** *pea3* and *cxcr7b* RNA smFISH in deposited mosaic organ progenitors with FGF3 induced (Fgf3-GFP/lyn-RFP/nls-tdTomato) cell clones (red) among cldnb:lyn-GFP labeled neighbor cells (green). RNA spots identified by 3D segmentation are shown in yellow if located within FGF-expressing clones, or in white if in surrounding cells of the same organ progenitor. Red outlines in the right panels indicate the positions of the Fgf3-expressing clones. Box plots show the quantification of *pea3* and *cxcr7b* levels per cell in deposited organ progenitors contrasting FGF expressing clones and the rest of the cells in the same organ progenitor (n = 5, 11, 6; n = 10, 13, 7; Wilcoxon test, ***P < 0.001). Scale bar: 5 µm.

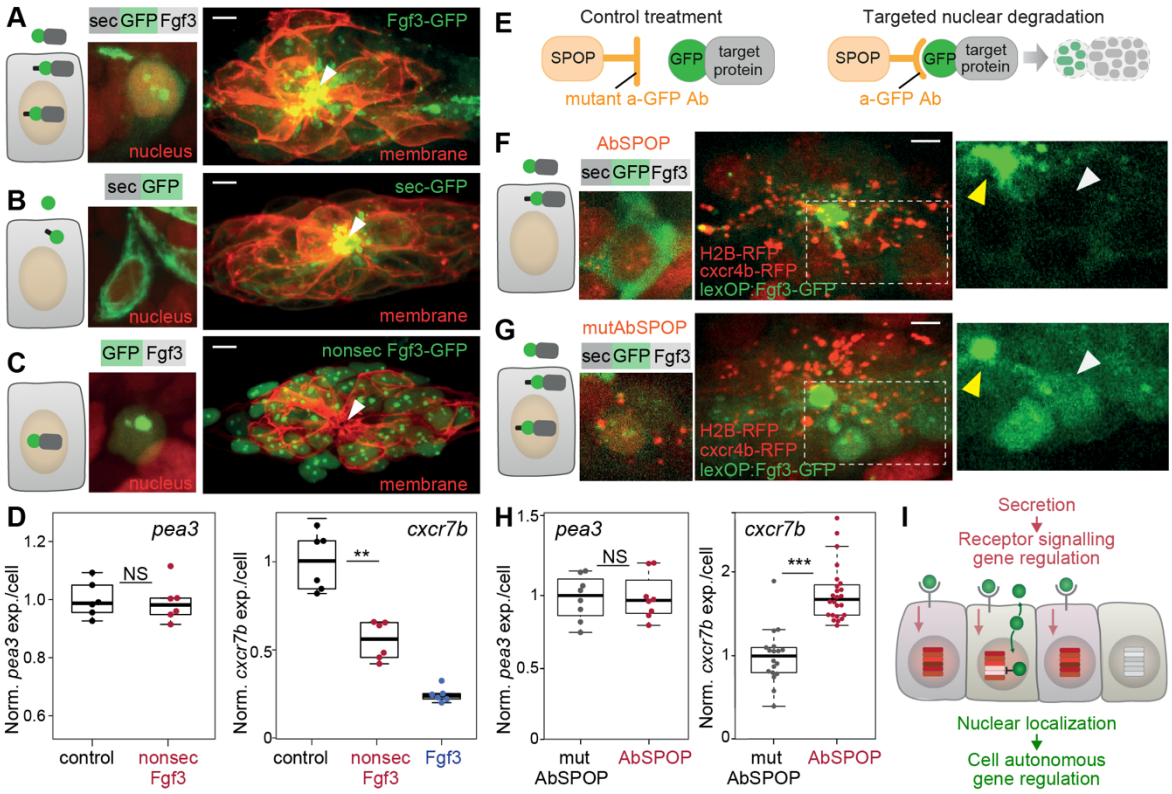

Figure 6. Nuclei localization of Fgf3 in its source cells has a distinct impact on gene expression than its signaling function.

A, B, C. Localization of GFP-tagged Fgf3 constructs. Fgf3-GFP (sec-GFP-Fgf3) represents full-length Fgf3, tagged with GFP between the signal peptide and the globular domain. sec-GFP is GFP-tagged signal peptide and nonsec-Fgf3-GFP (GFP-Fgf3) is GFP-tagged globular domain of Fgf3 without the signal peptide. Left panels show the illustration of the cellular localizations. Middle panels show the cellular imaging of the tagged proteins (green) with nuclear counter-label (nls-tdTomato, red). Right panels show the multicellular imaging of the GFP-tagged proteins (green) in assembled organs with membrane counter-label (lyn-RFP). Arrowheads point to the extracellular space in rosette centers (microlumen). **D**. Left panel shows the boxplot for *pea3* expression levels upon nonsec-Fgf3-GFP expression in organ progenitors**.** Right panel shows the boxplot for *cxcr7b* expression levels upon nonsec-Fgf3-GFP and Fgf3-GFP expression (*n* = 6 each). **E.** Description of the anti-GFP nanobody targeted nuclear degradation, where nuclei-localized protein population is targeted to degradation upon recognition of GFP tag via AbSPOP. Mutant anti-GFP nanobody-SPOP fusion serves as non-targeting control (mutAbSPOP). **F, G.** Fgf3-GFP localization upon lexop:fgf3-gfp expression with targeted nuclear degradation (F) versus non-targeting (G). Left two panels show the illustration and imaging of the cellular localizations. Middle panels show the cellular imaging of the tagged proteins (green) with nuclear counter-label (nls-tdTomato, red). Right two panels show the multicellular imaging of the Fgf3-GFP (green) in organ progenitors with counter-labels (H2B-RFP and cxcr4b-RFP), and close-up views of the boxed regions for inspection of Fgf3-GFP cellular localization. Microluminal (extracellular space) and nuclear space are indicated with yellow and white arrows, respectively. **H,** *pea3* and *cxcr7b* expression levels in control and nuclear degraded Fgf3-GFP expressing organ progenitors (*n* = 8 for each group; *n* =

18 and 24, respectively)**. I.** Schematic representation of the FGF driven gene expression regulation model. Scale bars: (A-C, F-G) 5 μm. Statistics: Wilcoxon test, $^{**}P < 0.01$, $^{***}P < 0.001$.

Supplemental Figures

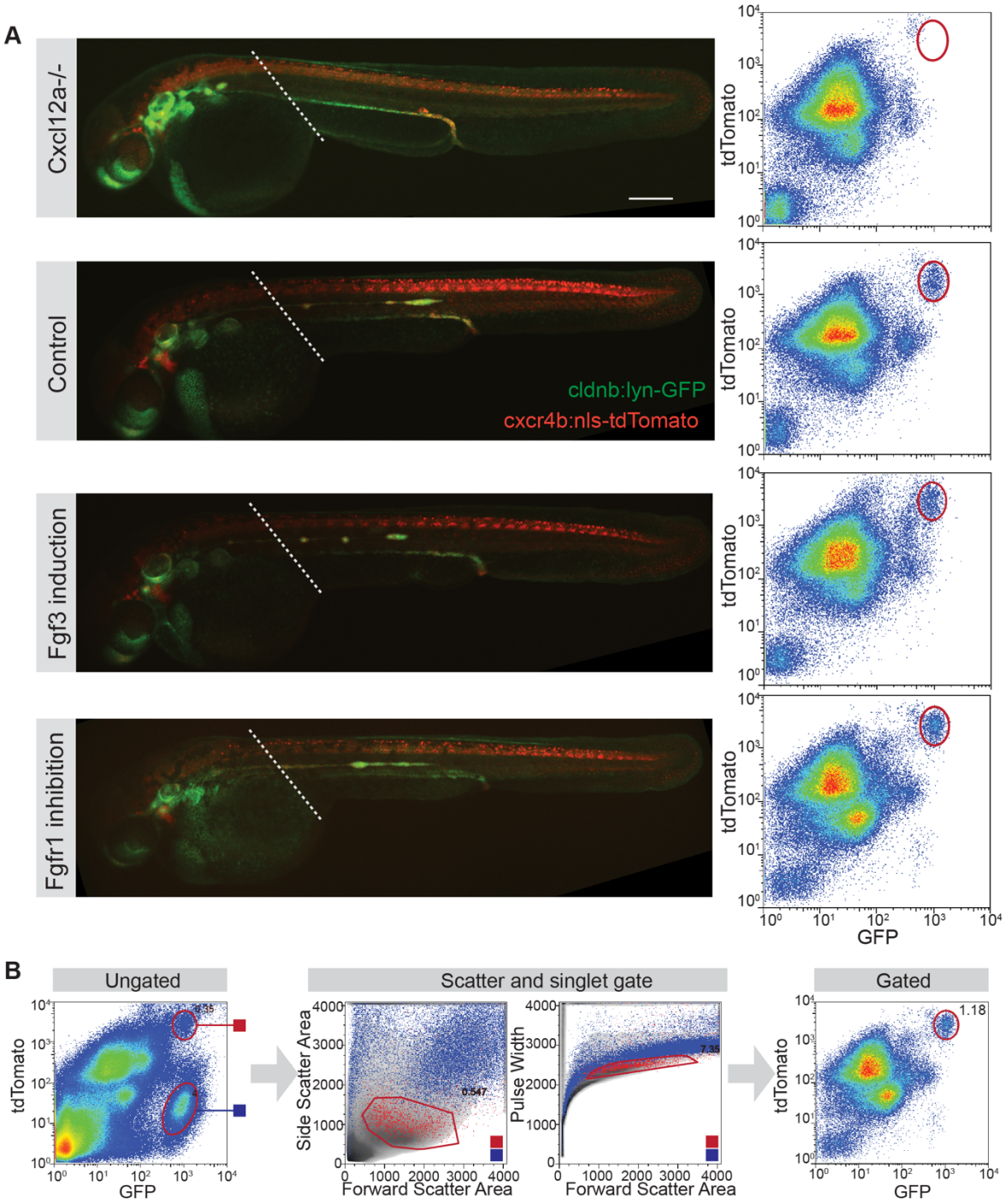

Figure S1. Identification and isolation of the lateral line cells with FACS.
A. (Left) whole embryo images of cxcl12a (sdf1a) mutant, wild-type, Fgf3-induced and Fgfr1 inhibited transgenic cldnb:lyn-GFP, cxcr4b:nlsTomato embryos at 30 hpf. Dashed lines indicate the site of dissection to isolate trunks. (Right) Corresponding fluorescence density plots (blue to red: low to high density of cell counts) showing the gated cells, dissociated from the trunks. The sorted LLP population is circled, which is absent in Cxcl12a mutants due to the impaired primordium migration towards the trunk of the embryo. **B.** Description of the sorting gates to isolate lateral

line primordium cell population from the rest of the fish trunks. Ungated: All the cells in the embryo trunks are plotted by their tdTomato and GFP fluorescence signal. The regions corresponding to the reference population (blue box) and the primordium population (red box) are outlined. Scatter and singlet gate: Scatter plots of all the cells in grey density representation. Primordium population (red dots) and reference population (blue dots) are overlaid on the plots. Gates used to sort LLP are outlined with red lines. Gated: Fluorescence plot of remaining cells after the scatter and singlet gates. Sorted primordium population is outlined in red. Scale bar, (A) 200 μm.

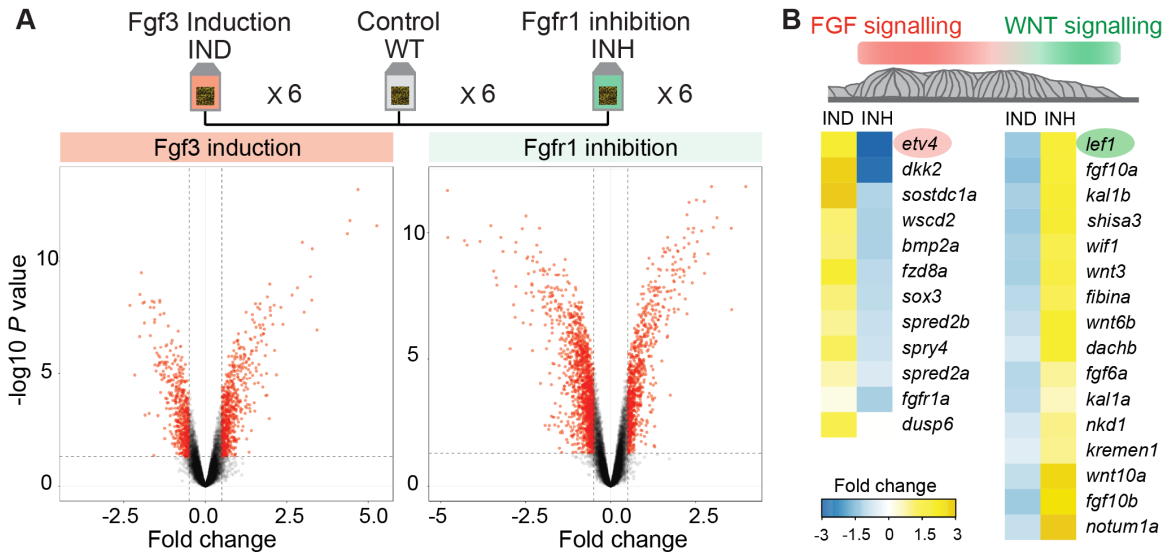

Figure S2. Fgf3 misexpression and Fgfr1 inhibition leads to differential gene regulation in LLP, impacting the known FGF and WNT signaling targets.
A. Description of gene expression profiling of Fgf3 induction, wild-type, and Fgfr1 inhibition, across six biological replicates. Volcano plots show the thresholds used to identify genes that are differentially expressed under treatment conditions relative to the control. **B.** Differential regulation of FGF (red) and WNT (green) signaling players in lateral line primordium. Heatmaps show the fold changes in comparison to wild-type levels (blue: down-regulation, yellow: up-regulation).

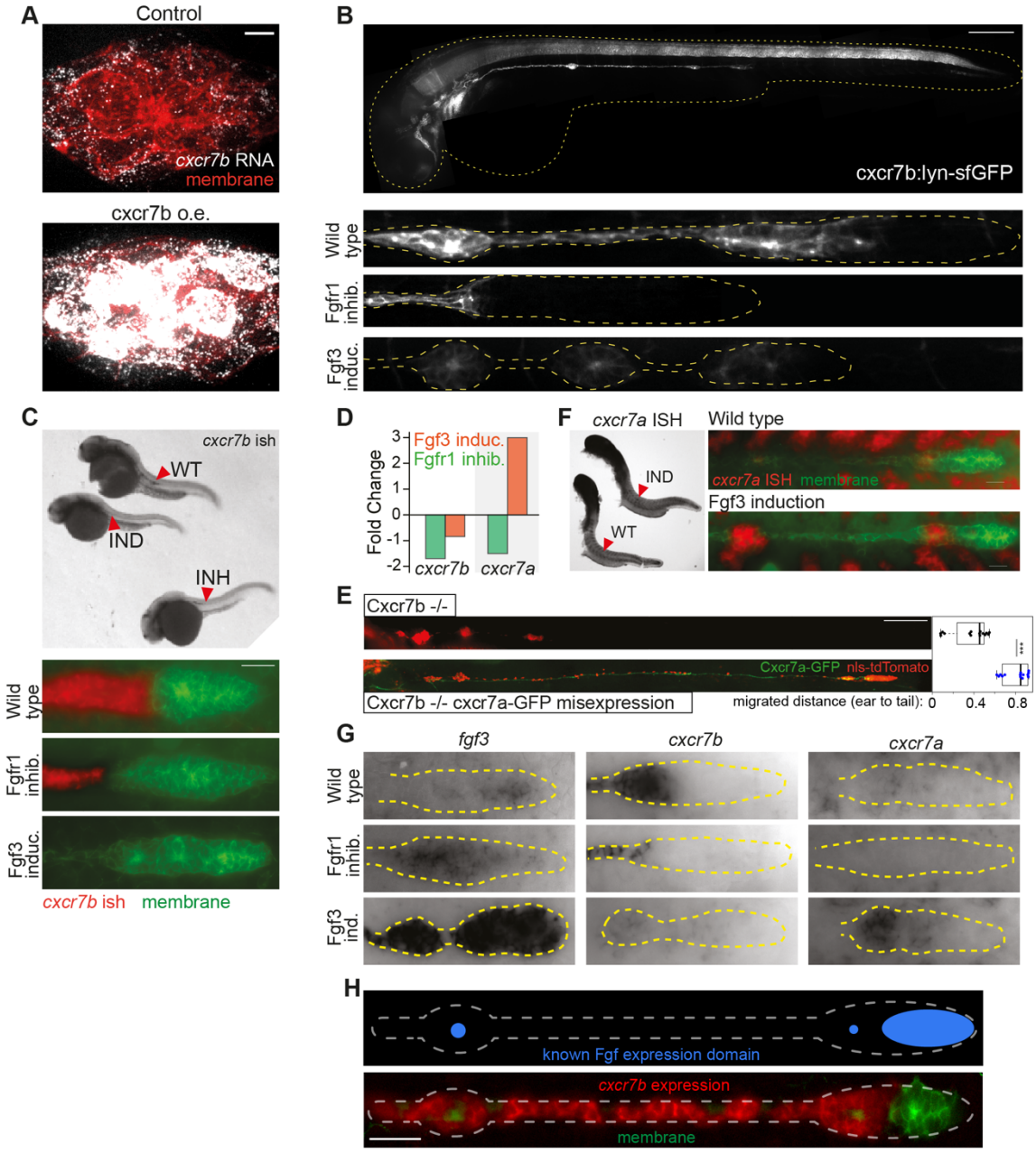

Figure S3. Impact of FGF manipulations on gene expression of *cxcr7b*.
A. Establishing *cxcr7b* smFISH (grey) using control (cxcr4b:lexPR) and *cxcr7b* overexpressing (cxcr4b:lexPR/lexOP:cxcr7b) lateral line organs (cldnb:lyn-GFP, red), confirming the specific recognition of *cxcr7b* mRNA by the smFISH probes. **B.** Whole embryo image of cxcr7b:lyn-sfGFP (white) transgenic line marking the *cxcr7b* expression domains with membrane-GFP (thus a low turn-over rate of the reporter). Lower panels: Close-up images of the lateral line in cxcr7b:lyn-sfGFP embryos, showing responses to early FGF induction and inhibition. **C.** *cxcr7b* colorimetric RNA in situ hybridization (ISH) of whole embryos (black) and close-up (red) images upon FGF manipulations (cldnb:lyn-GFP, green). **D.** Bar plots showing the change in gene expression of *cxcr7b* and *cxcr7a* paralogs upon FGF induction and Fgfr1 inhibition, probed by the microarrays. **E.** Rescue of Cxcr7b loss-of-function by Cxcr7a in cell migration. Upper panel: 2-day-old Cxcr7b mutant embryo where primordium failed to migrate. Lower panel: transient Cxcr7a-GFP expression (gal4/uas:cxcr7a-GFP) that

rescues the primordium migration. Scale bar, 200 µm. Migration quantified (n = 15 for control, 14 for rescue). **F.** *cxcr7a* colorimetric ISH (black) on wild-type and Fgf3 induced embryos, showing increased *cxcr7a* expression at lateral line organ progenitors upon Fgf3 induction. Right, close-up images of the lateral line with cldnb:lyn-GFP counter-label. **G.** *fgf3*, *cxcr7b* and *cxcr7a* ISH (black) on wild-type, Fgfr1 inhibited and Fgf3 induced lateral line primordium, highlighting the opposite response of *cxcr7b* and *cxcr7a* to FGF induction where all the cells express Fgf3 ligand. **H.** Opposing expression pattern of FGF signaling target *cxcr7b* with the known FGF ligand expression pattern (red: *cxcr7b* ISH, green: cldnb:lyn-GFP membrane label, blue schema: known FGF ligand expression) in the zebrafish lateral line. Scale bars: (A) 5 µm, (B) 200 µm, (C) 20 µm, (H) 50 µm. Statistics: Wilcoxon test, ***$P < 0.001$.

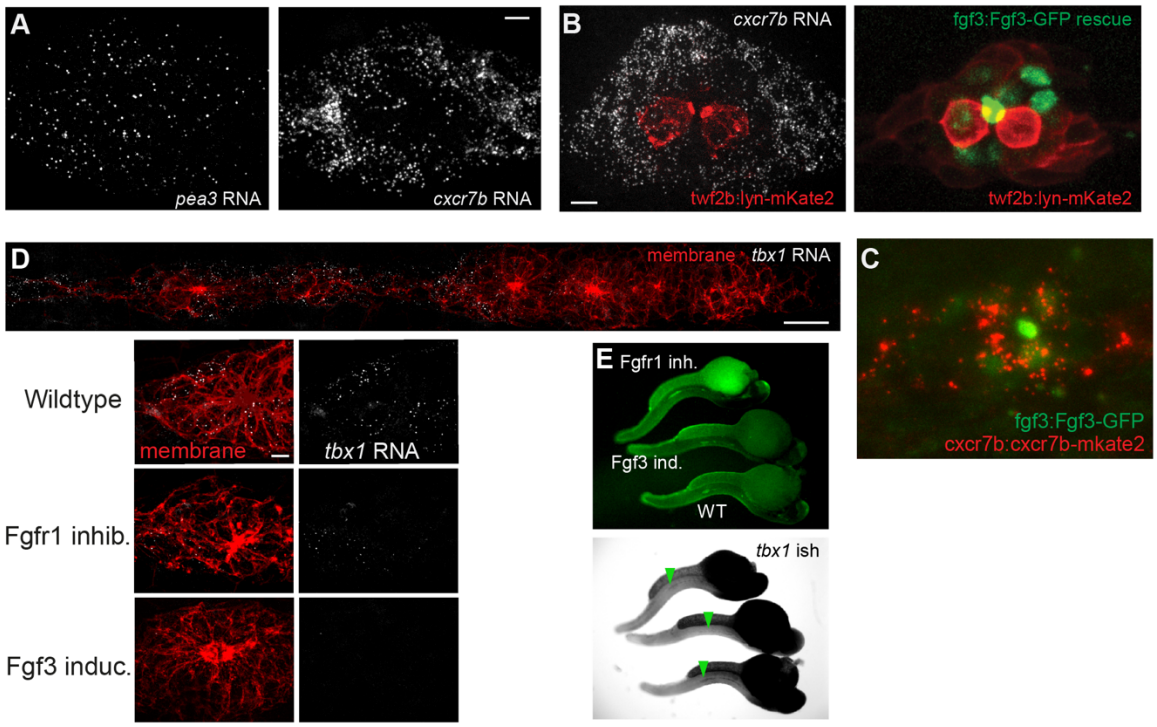

Figure S4. Probing cxcr7b and tbx1 gene expression patterns in comparison to Fgf3.

A. Single smFISH channels of Figure 2B. **B.** Composite images of *cxcr7b* smFISH (white) and fgf3:Fgf3-GFP rescue (green) from Figure 2D, overlaid with the membrane marker of twf2b:lyn-mKate2 (red) to facilitate 3D alignment of the two imaging sets from the same organ progenitor. **C.** Composite image of a lateral line organ progenitor marked with cxcr7b:Cxcr7b-mkate2 (red) *and* fgf3:Fgf3-GFP (green). The cellular *cxcr7b* gene expression pattern cannot be resolved using the endogenously tagged Cxcr7b protein due to its high turnover in the lateral line cells (seen as punctate signal), in contrast to the other tissues shown in Figure 3B. **D.** *tbx1* RNA smFISH (white) on the lateral line (red, cldnb:lyn-GFP) and its response to the FGF manipulations at the trailing edge of the primordium, a pattern similar to that of *cxcr7b*. **E**. Colorimetric ISH (black) of *tbx1* on whole fish embryos (cldnb:lyn-GFP, green) in response to FGF manipulations. Arrows point to lateral line primordium. Scale bars: (A, B, D-lower panel) 5 µm, (D-upper panel) 20 µm.

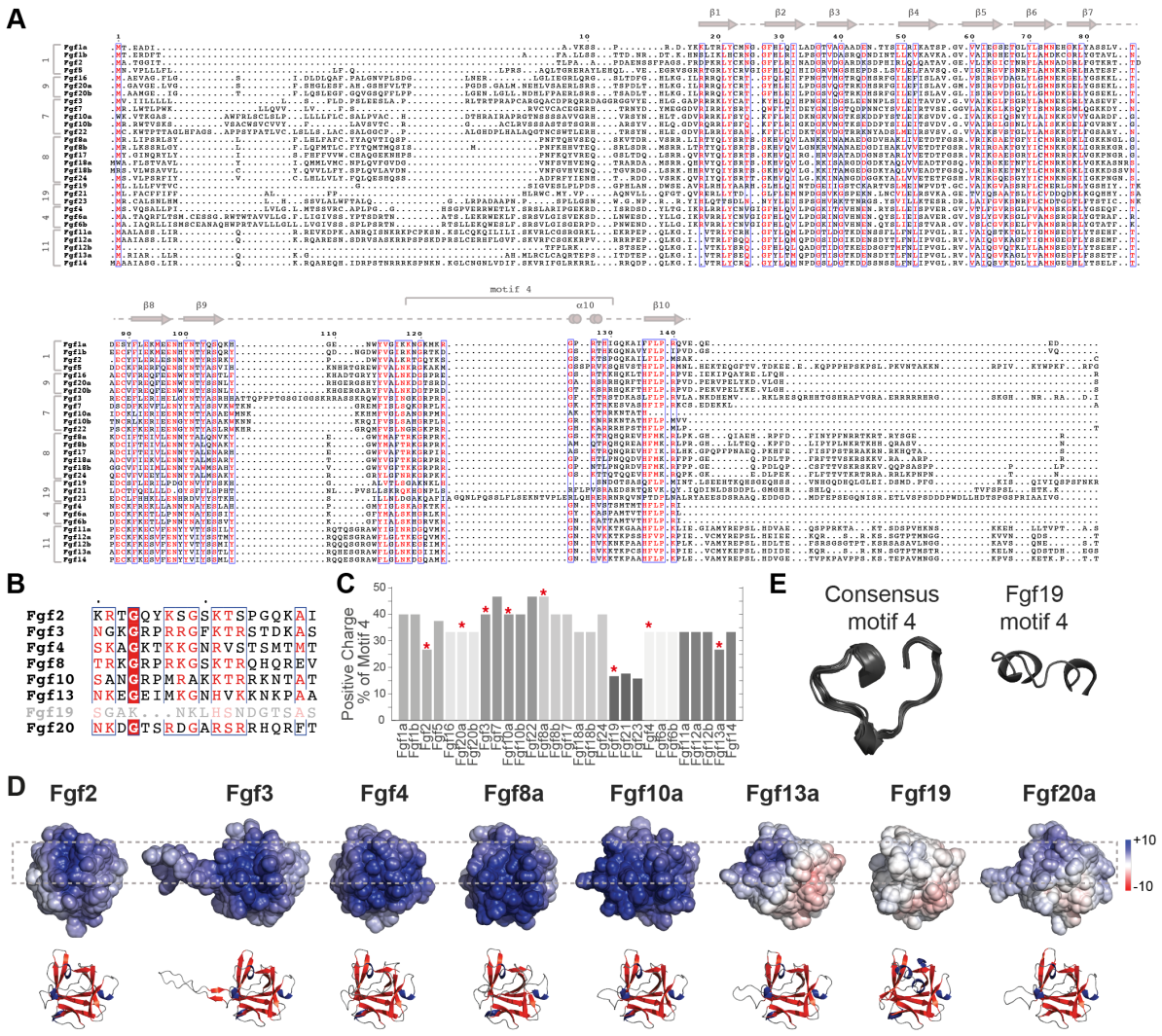

Figure S5. Comparative sequence and structural analysis of zebrafish FGFs. **A.** Multiple sequence alignments of zebrafish FGFs performed using the T-Coffee server[52] and visualized with ESPript 3.0[53]. If the score is greater than SimilarityGlobalScore, it is in red characters, and strictly conserved residues appear as white characters on a red background. A previously predicted motif-4[39] is highlighted due to its potential to provide a nuclear localization signal that is positively charged, in an extended-exposed conformation and conserved. **B. A** closer look at the sequence conservation of motif-4 among the experimentally tested FGFs. **C**. Positive charge percentage of motif-4 among FGFs. FGFs tested experimentally are marked with a star. **D.** Electrostatic surface maps of zebrafish FGFs, with structures predicted by AlphaFold3.0. Surface charge scale spans from -10 (red) to +10 (blue)**.** The region corresponding to motif-4 is boxed, which shows a highly positively charged domain on the surface of the FGFs except Fgf19. **E.** Closer inspection of the motif further showed that its 3D structure was conserved except for Fgf19.

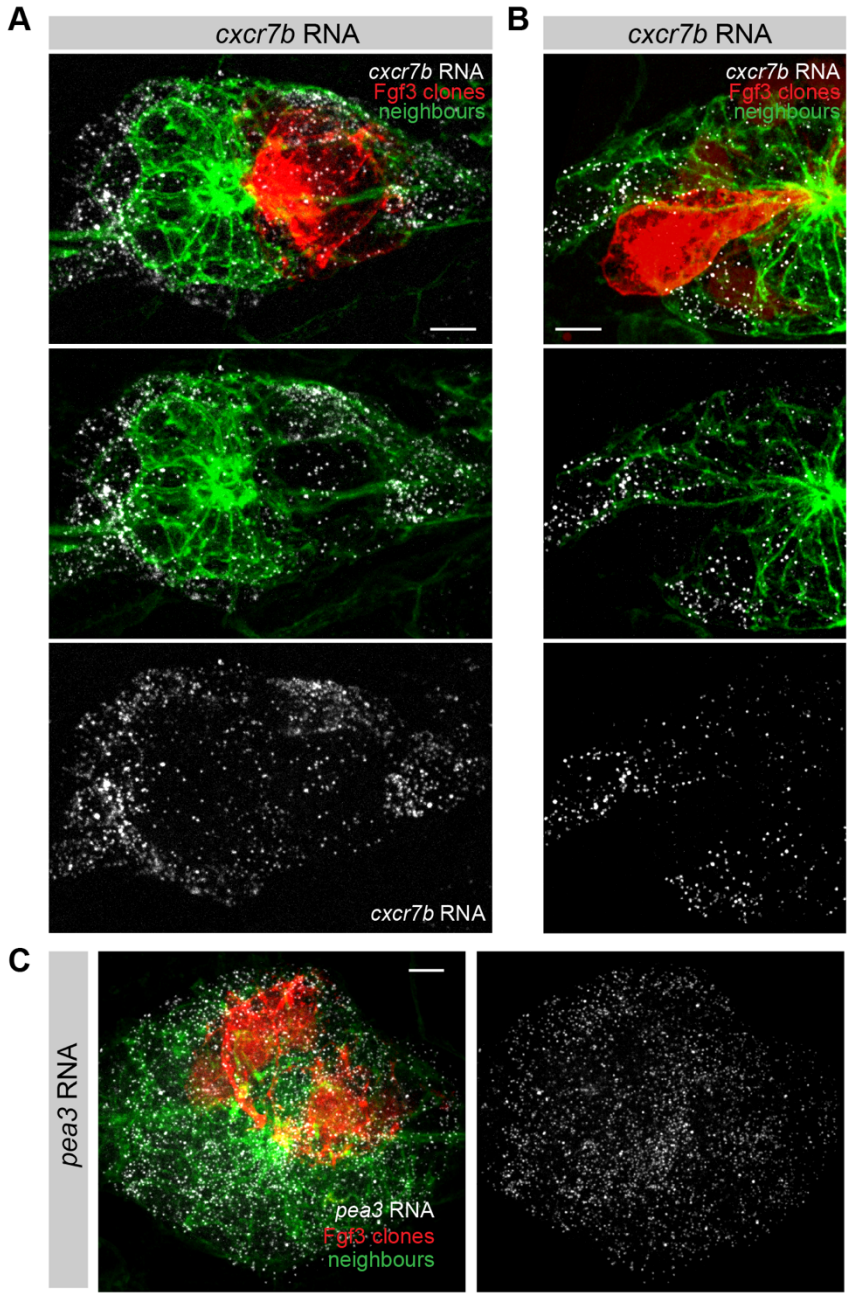

Figure S6. Clonal Fgf3 misexpression demonstrates the cell autonomous repression of *cxcr7b*.

A, B. Maximum Z-projections of *cxcr7b* smFISH (white) following clonal Fgf3 misexpression (red) and the cells around them (green) in a mature organ progenitor (A) and at the trailing end of a primordium (B). **C.** *pea3* smFISH (white) on Fgf3 misexpression clones (red) along with surrounding cells (green) in a mature organ progenitor. Scale bars: (A-C) 5 µm.

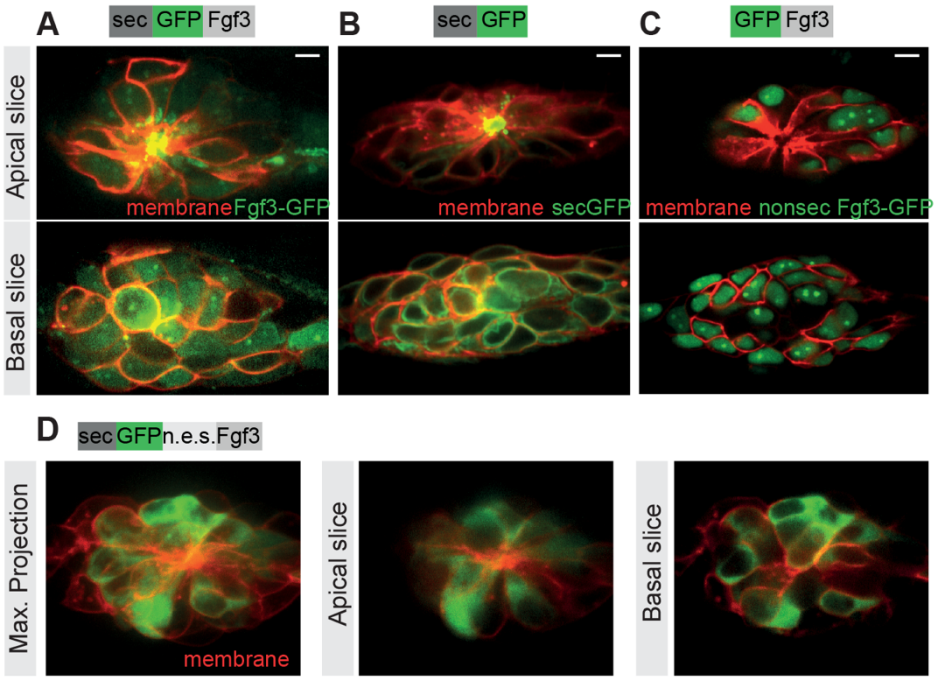

Figure S7. Cellular localization of Fgf3 constructs in lateral line organ progenitors.

A-C. Apical and basal slices of the imaged organ progenitors as shown in Figure 6A-C, highlighting the corresponding extracellular (apical lumen in the rosette center) and cellular localizations within the lateral line organ progenitors. Scale bars: 5 µm.
D. Apical, basal slices, and the maximal projected images of a Fgf3-GFP construct tagged with a nuclear export signal (n.e.s), showing anticipated absence of nuclear Fgf3 and unintended block of Fgf3 localization to the extracellular space.

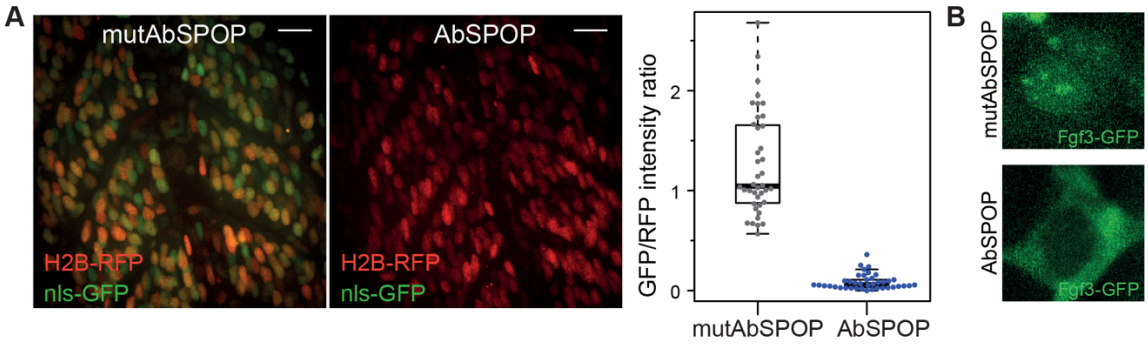

Figure S8. Establishing a nuclear-targeted GFP degradation system for selective depletion of nuclear Fgf3-GFP.

A. Specificity and efficiency of the anti-GFP degradation tested in zebrafish somites with triple RNA injections of H2B-RFP (red), nlsGFP (green) and either mutAbSPOP or AbSPOP. Left panels show the corresponding example images, and right panel shows the intensity measurements. **B.** Cellular localization image of Fgf3-GFP (green channel of Figure 6F-G) upon control (mutAbSPOP) treatment and nuclear degradation (AbSPOP). Scale bars: (A) 20 μm.

Methods

Zebrafish handling and stocks

Zebrafish (Danio rerio) strains were maintained as described in Westerfield[54]. Embryos were raised in E3 buffer between 26-30°C. All experiments were conducted on embryos younger than 3 dpf, under the guidelines of the European Commission, Directive 2010/63/EU. All chemical treatments were conducted on embryos that were dechorionated with pronase. Embryos were anesthetized with 0.01% Tricane for live imaging and anesthetized before dissection and chemical fixation procedures. To prevent pigmentation when required, embryos were treated with 0.002% PTU at 24 hpf. To perform live imaging, embryos were mounted with 0.8% LMP agarose on glass bottom dishes (MatTek) and kept at 28°C. Following established mutants and transgenics were used: cxcl12a^{t30516} from Valentin *et al.* [35], cxcr4b:nls-tdTomato from Donà *et al.*[30], cldnb:lyn-GFP[25], gal4(ETLGA346) uas:mCherry[55], atoh:tdTomato[56], uas:Cxcr7b-GFP[30], cxcr4b:lexPR/lexop:lyn-RFP , lexop:Fgf3-GFP, lexop: secGFP, fgf3:Fg3-GFP and cxcr4b:cxcr4b-tagRFP from Durdu *et al.*[29].

Constructs and Transgenic generation

LexOP and UAS responder lines were generated using multisite-gateway cloning (Invitrogen) and the Tol2kit[57]: i) LexOP(p5E)/GFP(pME)/fgf3(p3E), ii) UAS(p5E)/cxcr7a(pME)/GFP(p3E), iii) LexOP(p5E)/cxcr7b(pME)/GFP(p3E), iv) LexOP(p5E)/caFgfr1(pME)/RFP(p3E), v)LexOP(p5E)/Mycn(pME)/GFP(p3E). All destination vectors carry SV40poly(A) at C terminus in the final construct. As a transgenic marker, all clones carry cmlc2:eGFP cassette at the backbone.

ca-Fgfr1a was cloned using the construct of hs:caFgfr1 from Marques *et al.*[58]. FGF family and *cxcr7a* cDNAs were generated from total RNA extracts of zebrafish embryos at 30 hpf. FGF ORFs were cloned in CMV plasmids where GFP is inserted after the signal peptide, same as Fgf3.

twf2b:lyn-mKate2 was generated by inserting lyn-mKate2 in Twf2b BAC clone CH211-14I3 replacing the first exon. cxcr7b:cxcr7b-mKate2 was generated by inserting mKate2 in cxcr7b BAC clone DKEY-96H14 and cxcr7b:lyn-sfGFP was generated by inserting lyn-sfGFP in *cxcr7b* BAC clone replacing the first exon. Recombinations were done by ET recombineering (Gene Bridges). As the transgenic marker, cry:FP/KanR cassette was inserted in the BAC backbone, which drives the expression of FPs in the eye lens. BACs were purified with Large Construct Kit, Qiagen and transgenic lines were generated by injecting the constructs at one-cell stage.

Colorimetric In-Situ Hybridization (ISH)

pea3, *fgf3* and *cxcr7 in situ* hybridization (DIG probes, anti-DIG Alkaline Phosphatase coupled antibody, NBT/BCIP substrate at 30°C) were performed as described previously[28,35]. *cxcr7a in situ* hybridization was performed with standard protocols, using probes generated from *cxcr7a* cDNA. All in-situ probes were

hybridized at 65°C. To counter-label primordium, anti-GFP antibody staining (rabbit-anti GFP primary antibody with Alexa488-anti-rabbit secondary antibody) was performed on cldnb:lyn-GFP transgenic embryos during ISH protocol as in Valentin *et al.*[35].

Fluorescence Recovery After Photobleaching

Fluorescence Recovery After Photobleaching (FRAP) experiments were performed using an Ultraview VoX spinning disk microscope equipped with a photokinesis unit and Zeiss ×63 water objective. To monitor fluorescence recovery after photobleach, 5 pre-bleach and 45 post-bleach images were acquired at a speed of 30 msec per frame. Bleached region was defined with a strip ROI at the edge of the pool. Mean intensity signal over time within the bleached region, total pool and the background were measured to calculate half time of recoveries. The measurements were imported to easyFRAP software[59] and the recovery curves were analyzed with full-scale normalization and double term fitting.

Single molecule fluorescence *in situ* hybridization

Single molecule fluorescence *in situ* hybridization (smFISH) probes (Custom Stellaris FISH probes, Biosearch Technologies) of *pea3* (*etv4*), *cxcr7b* and *tbx1* were designed by Stellaris RNA FISH probe designer, composed of minimum 40 sequence specific oligonucleotides (each 20bp). Probes were conjugated to either Cal Fluor 590 (red) or Quasar 670 (far red) fluorophores. Hybridization, imaging and analysis were performed as described before[29].

Clonal and transient misexpression

Established cell transplantation protocols[54] were used to generate Fgf3-GFP misexpression cell clones. Donor cells of cxcr4b:LexPR, lexOP:lyn-RFP, lexOP:Fgf3-GFP, cxcr4b:nls-tdTomato transgenic embryos were transplanted into cldnb:lyn-GFP transgenic embryos. To induce expression of Fgf3-GFP, embryos were treated with 10 μM RU486 at 24 hpf.

Misexpression clones of caFgfr1 were generated by injection of lexOP:caFgfr1-RFP construct in cxcr4b:LexPR, cldnb:lyn-GFP transgenic embryos at one cell stage. The expression was induced by 10 μM RU486 treatment at 24 hpf. RNA injection method at single cell stage was used to express H2B-RFP, nls-GFP, AbSPOP[46] and mutAbSPOP encoding mRNAs that were generated with in vitro transcription (Ambion mMessage mMachine Kit) using linearized SP6 or T7 containing plasmids. Transient expression of GFP-tagged *fgf2*, *fgf3*, *fgf4*, *fgf8*, *fgf10*, *fgf13*, *fgf19 and fgf20* in early embryos were achieved by the injection of the CMV promoter DNA constructs together with in vitro transcribed H2B-RFP RNA at single cell stage.

Gene expression profiling

Three experimental groups were used for gene expression profiling. i) Wild type group was cldnb:lyn-GFP, cxcr4b:nls-tdTomato transgenics incubated with 10 μM RU486, 0.1% DMSO. ii) FGF inhibition group was cldnb:lyn-GFP, cxcr4b:nls-

tdTomato transgenics, incubated with 1 μM SU5402, 0.1% DMSO, 10 μM RU486. iii) FGF induction group was cldnb:lyn-GFP, cxcr4b:nls-tdTomato, cxcr4b:LexPR, lexOP:Fgf3-GFP transgenics, incubated with 10 μM RU486, 0.1% DMSO. Embryos at 24 hpf stage were treated with inducers and inhibitors for 6 hours. For each sample at least 300 transgenic embryos were used. Embryos were dissected with a scalpel by separating trunks and collected in 2 ml tubes. Embryos were dissociated with FACSmax (Genlantis) and passed through 40 μm cell strainer. Around 20000 cells were sorted with FACS using the GFP, RFP and scatter gates, identified by the absence of the lateral line cell population in cxcl12a mutant embryos. Total RNA was extracted with Qiagen RNeasy kit and stored at -80°C. RNA quality was validated and the concentration was measured with Qubit. Samples were processed as described in Affymetrix GeneChip System Protocol and hybridized to Zebrafish Gene ST 1.0 arrays.

Analysis of the microarray data

Affymetrix Power Tools (APT) was used to pre-process and normalize cel files generated for each sample. Expression values of 'meta' probe sets (transcripts) were summarized with the Robust Microarray Analysis (RMA) approach[60] as implemented in APT (log2 transformed). The quality control of the samples was initially carried out by checking chips with outlier values of 'average raw intensity signal' and 'mean absolute deviation of the residuals'. Detected above background (DABG) method was applied to estimate whether probe sets were higher than the background distribution. As recommended[61], 'main/meta' probe sets were retained if half or more of the associated probe sets were detected (DABG, P value<0.05) in at least half of the replicates of any experimental condition[62,63]. Out of 40,344 'main/meta' probe sets, 24,720 'main/meta' probe sets were selected for further analysis as they were annotated with the corresponding gene symbols (21,446 unique) derived from the Affymetrix-ZebGene-1_0-st-v1.na34.zv9.transcript data and through manual curation. Unsupervised hierarchical clustering of the samples (Pearson's correlation coefficient, average-linkage) was performed to examine outliers and batch effect. limma package[64] (Smyth, 2004) available from Bioconductor[65] was used to identify differentially expressed genes for the comparisons of the biological groups while accounting for the batch of the replicate experiments. False discovery rate (FDR) was applied for multiple-test correction[66]. Heat maps representing the fold-changes in figures were generated in R.

Protein structure models

Protein sequences of all FGF family members were compared using multiple sequence alignment performed with the T-Coffee server[52], and visualized using the ESPript 3.0 server[53]. For protein structure modeling, protein sequences for Fgf2, Fgf3, Fgf4, Fgf8a, Fgf10a, Fgf13a, Fgf19, and Fgf20a were retrieved from the SMART database[67], selecting the "Acidic and basic fibroblast growth factor family" domains. Structural models were generated using AlphaFold3[68] (https://alphafoldserver.com/) with default parameters, and model confidence was

assessed via per-residue pLDDT scores. Electrostatic surfaces were computed using APBS[69] via server (https://server.poissonboltzmann.org/) after preprocessing with pdb2pqr[70] under standard settings. All models were superimposed in PyMOL[71] (v2.5.0) using the align function, and electrostatic surfaces and structural features were visualized using custom PyMOL scripts. The classical NLS signal was characterized to be rich in positively charged amino acids and found to be exposed, in an extended loop conformation[72] . With this consideration, we focused on the conserved site (motif 4[39]) in Fgf3 that has such structural potential. We compared this site among FGF zebrafish family with multiple sequence alignment. We inspected this motif further on the 3D structures for its charge, exposure and structure.

Statistical analysis

All the statistical analysis was carried out using R[73]. A non-parametric Wilcoxon rank-sum test (two sided) was used to compare two groups. Sample sizes (n) and *P* values (*P*) for each experiment are listed below and indicated in figures (*$P < 0.05$,**$P < 0.01$,***$P < 0.001$).

Boxplots are standard box and whisker plots showing median and interquartile range. For all the experiments, original data points were displayed as scatter plots on top of boxplots using the beeswarm package, allowing direct examination of the variance and distribution of the samples. Scatter and line figures were generated using the ggplot2 R package[74].

P values and sample sizes:

Figure 1C: $n_{WT} = 4$, $n_{FGFRinh} = 5$, $n_{FGFind} = 6$, ~40 cells per fish**,** $P_{WT\text{-}FGFRinh} = 0.015$, $P_{WT\text{-}FGFind} = 0.0095$, $P_{FGFRinh\text{-}FGFind} = 0.051$. **Figure 4B:** *pea3* expression: $n_{ctrl} = 5$, $n_{FGF} = 11$, $n_{neigh} = 6$, $P_{ctrl\text{-}FGF} = 4.6 \times 10^{-4}$, $P_{ctrl\text{-}neigh} = 4.3 \times 10^{-3}$, $P_{FGF\text{-}neigh} = 0.88$; *cxcr7* expression: $n_{ctrl} = 10$, $n_{FGF} = 13$, $n_{neigh} = 7$, $P_{ctrl\text{-}FGF} = 1.7 \times 10^{-4}$, $P_{ctrl\text{-}neigh} = 0.53$, $P_{FGF\text{-}neigh} = 1.2 \times 10^{-3}$. **Figure 5D:** Calculated mobile fraction: nls-GFP 0.98, Fgf3-GFP 0.83, Mycn-GFP 0.86; $t_{1/2}$ (s): nls-GFP 0.24, Fgf3-GFP 0.95, Mycn-GFP 0.97. **Figure 6D**: $n_{ctrl} = 6$, $n_{nonsecFgf3} = 6$, $n_{Fgf3} = 6$, *pea3*: $P_{ctrl\text{-}nonsecFgf3} = 4.6 \times 10^{-4}$; *cxcr7b:* $P_{ctrl\text{-}nonsecFgf3} = 2.2 \times 10^{-3}$, $P_{ctrl\text{-}Fgf3} = 2.2 \times 10^{-3}$, $P_{nonsecFgf3\text{-}Fgf3} = 2.2 \times 10^{-3}$. **Figure 6H**: *pea3*: $n_{mutAbSPOP} = 8$, $n_{mutAbSPOP} = 8$, $P_{Pea3} = 1$; *cxcr7b*: $n_{mutAbSPOP} = 18$, $n_{mutAbSPOP} = 24$, $P_{Cxcr7b} = 1.1 \times 10^{-8}$. **Figure S3E:** $n_{cxcr7b\text{-}/\text{-}} = 15$, $n_{cxcr7b\text{-}/\text{-}\ uas\mathit{Cxcr7}amisexp} = 14$, $P_{(cxcr7b\text{-}/\text{-})\text{-}(cxcr7b\text{-}/\text{-}\ uas\mathit{Cxcr7}amisexp)} = 2.6 \times 10^{-8}$.

References

1. Li, P., and Elowitz, M.B. (2019). Communication codes in developmental signaling pathways. Development *146*. https://doi.org/10.1242/DEV.170977.
2. Hill, C.S., and Treisman, R. (1995). Transcriptional regulation by extracellular signals: mechanisms and specificity. Cell *80*, 199–211. https://doi.org/10.1016/0092-8674(95)90403-4.
3. Perrimon, N., Pitsouli, C., and Shilo, B.Z. (2012). Signaling mechanisms controlling cell fate and embryonic patterning. Cold Spring Harb Perspect Biol *4*. https://doi.org/10.1101/CSHPERSPECT.A005975.
4. Martin, G.R. (1998). The roles of FGFs in the early development of vertebrate limbs. Genes Dev *12*, 1571–1586. https://doi.org/10.1101/GAD.12.11.1571.
5. Böttcher, R.T., and Niehrs, C. (2005). Fibroblast growth factor signaling during early vertebrate development. Endocr Rev *26*, 63–77. https://doi.org/10.1210/ER.2003-0040.
6. Dorey, K., and Amaya, E. (2010). FGF signalling: diverse roles during early vertebrate embryogenesis. Development *137*, 3731–3742. https://doi.org/10.1242/DEV.037689.
7. Ornitz, D.M., and Itoh, N. (2015). The Fibroblast Growth Factor signaling pathway. Wiley Interdiscip Rev Dev Biol *4*, 215–266. https://doi.org/10.1002/WDEV.176.
8. Sagner, A., and Briscoe, J. (2017). Morphogen interpretation: concentration, time, competence, and signaling dynamics. Wiley Interdiscip Rev Dev Biol *6*. https://doi.org/10.1002/WDEV.271.
9. Kicheva, A., and Briscoe, J. (2023). Control of Tissue Development by Morphogens. Annu Rev Cell Dev Biol *39*, 91–121. https://doi.org/10.1146/ANNUREV-CELLBIO-020823-011522.
10. Mosby, L.S., Bowen, A.E., and Hadjivasiliou, Z. (2024). Morphogens in the evolution of size, shape and patterning. Development *151*. https://doi.org/10.1242/DEV.202412.
11. Stapornwongkul, K.S., and Vincent, J.P. (2021). Generation of extracellular morphogen gradients: the case for diffusion. Nat Rev Genet *22*, 393–411. https://doi.org/10.1038/S41576-021-00342-Y.
12. Bertrand, V., Hudson, C., Caillol, D., Popovici, C., and Lemaire, P. (2003). Neural Tissue in Ascidian Embryos Is Induced by FGF9/16/20, Acting via a Combination of Maternal GATA and Ets Transcription Factors. Cell *115*, 615–627. https://doi.org/10.1016/S0092-8674(03)00928-0.
13. Brent, A.E., and Tabin, C.J. (2004). FGF acts directly on the somitic tendon progenitors through the Ets transcription factors Pea3 and Erm to regulate scleraxis expression. Development *131*, 3885–3896. https://doi.org/10.1242/DEV.01275.
14. Raible, F., and Brand, M. (2001). Tight transcriptional control of the ETS domain factors Erm and Pea3 by Fgf signaling during early zebrafish development. Mech Dev *107*, 105–117. https://doi.org/10.1016/S0925-4773(01)00456-7.
15. Roehl, H., and Nüsslein-Volhard, C. (2001). Zebrafish pea3 and erm are general targets of FGF8 signaling. Curr Biol *11*, 503–507. https://doi.org/10.1016/S0960-9822(01)00143-9.
16. Dailey, L., Ambrosetti, D., Mansukhani, A., and Basilico, C. (2005). Mechanisms underlying differential responses to FGF signaling. Cytokine Growth Factor Rev *16*, 233–247. https://doi.org/10.1016/J.CYTOGFR.2005.01.007.
17. Ingham, P.W., and McMahon, A.P. (2001). Hedgehog signaling in animal development: paradigms and principles. Genes Dev *15*, 3059–3087. https://doi.org/10.1101/GAD.938601.

18. Artavanis-Tsakonas, S., Rand, M.D., and Lake, R.J. (1999). Notch signaling: Cell fate control and signal integration in development. Science (1979) *284*, 770–776. https://doi.org/10.1126/SCIENCE.284.5415.770/ASSET/355D0AAB-3A6D-428F-B213-5F1C35A50AB7/ASSETS/GRAPHIC/SE1797476004.JPEG.
19. Lecuit, T., and Cohen, S.M. (1998). Dpp receptor levels contribute to shaping the Dpp morphogen gradient in the *Drosophila* wing imaginal disc. Development *125*, 4901–4907. https://doi.org/10.1242/dev.125.24.4901.
20. Ghysen, A., and Dambly-Chaudière, C. (2004). Development of the zebrafish lateral line. Curr Opin Neurobiol *14*, 67–73. https://doi.org/10.1016/j.conb.2004.01.012.
21. Ghysen, A., and Dambly-Chaudière, C. (2007). The lateral line microcosmos. Genes Dev *21*, 2118–2130. https://doi.org/10.1101/GAD.1568407.
22. Revenu, C., Streichan, S., Donà, E., Lecaudey, V., Hufnagel, L., and Gilmour, D. (2014). Quantitative cell polarity imaging defines leader-to-follower transitions during collective migration and the key role of microtubule-dependent adherens junction formation. Development *141*, 1282–1291. https://doi.org/10.1242/DEV.101675.
23. Thomas, E.D., Cruz, I.A., Hailey, D.W., and Raible, D.W. (2015). There and back again: development and regeneration of the zebrafish lateral line system. Wiley Interdiscip Rev Dev Biol *4*, 1–16. https://doi.org/10.1002/WDEV.160.
24. Chitnis, A.B., Dalle Nogare, D., and Matsuda, M. (2012). Building the posterior lateral line system in zebrafish. Dev Neurobiol *72*, 234–255. https://doi.org/10.1002/DNEU.20962.
25. Haas, P., and Gilmour, D. (2006). Chemokine signaling mediates self-organizing tissue migration in the zebrafish lateral line. Dev Cell *10*, 673–680. https://doi.org/10.1016/J.DEVCEL.2006.02.019.
26. Wang, J., Yin, Y., Lau, S., Sankaran, J., Rothenberg, E., Wohland, T., Meier-Schellersheim, M., and Knaut, H. (2018). Anosmin1 Shuttles Fgf to Facilitate Its Diffusion, Increase Its Local Concentration, and Induce Sensory Organs. Dev Cell *46*, 751-766.e12. https://doi.org/10.1016/j.devcel.2018.07.015.
27. Pines, O., Horwitz, M., and Herrmann, J.M. (2024). Privileged proteins with a second residence: dual targeting and conditional re-routing of mitochondrial proteins. FEBS J *291*, 5379–5393. https://doi.org/10.1111/febs.17191.
28. Lecaudey, V., Cakan-Akdogan, G., Norton, W.H.J., and Gilmour, D. (2008). Dynamic Fgf signaling couples morphogenesis and migration in the zebrafish lateral line primordium. Development *135*, 2695–2705. https://doi.org/10.1242/DEV.025981.
29. Durdu, S., Iskar, M., Revenu, C., Schieber, N., Kunze, A., Bork, P., Schwab, Y., and Gilmour, D. (2014). Luminal signalling links cell communication to tissue architecture during organogenesis. Nature *515*, 120–124. https://doi.org/10.1038/NATURE13852.
30. Donà, E., Barry, J.D., Valentin, G., Quirin, C., Khmelinskii, A., Kunze, A., Durdu, S., Newton, L.R., Fernandez-Minan, A., Huber, W., et al. (2013). Directional tissue migration through a self-generated chemokine gradient. Nature *503*, 285–289. https://doi.org/10.1038/NATURE12635.
31. Ma, E.Y., and Raible, D.W. (2009). Signaling pathways regulating zebrafish lateral line development. Curr Biol *19*. https://doi.org/10.1016/J.CUB.2009.03.057.
32. McGraw, H.F., Drerup, C.M., Culbertson, M.D., Linbo, T., Raible, D.W., and Nechiporuk, A. V. (2011). Lef1 is required for progenitor cell identity in the zebrafish lateral line primordium. Development *138*, 3921–3930. https://doi.org/10.1242/DEV.062554.
33. Aman, A., and Piotrowski, T. (2008). Wnt/beta-catenin and Fgf signaling control collective cell migration by restricting chemokine receptor expression. Dev Cell *15*, 749–761. https://doi.org/10.1016/J.DEVCEL.2008.10.002.

34. Dambly-Chaudière, C., Cubedo, N., and Ghysen, A. (2007). Control of cell migration in the development of the posterior lateral line: antagonistic interactions between the chemokine receptors CXCR4 and CXCR7/RDC1. BMC Dev Biol *7*. https://doi.org/10.1186/1471-213X-7-23.
35. Valentin, G., Haas, P., and Gilmour, D. (2007). The chemokine SDF1a coordinates tissue migration through the spatially restricted activation of Cxcr7 and Cxcr4b. Curr Biol *17*, 1026–1031. https://doi.org/10.1016/J.CUB.2007.05.020.
36. Nechiporuk, A., and Raible, D.W. (2008). FGF-dependent mechanosensory organ patterning in zebrafish. Science *320*, 1774–1777. https://doi.org/10.1126/SCIENCE.1156547.
37. Popovici, C., Roubin, R., Coulier, F., and Birnbaum, D. (2005). An evolutionary history of the FGF superfamily. Bioessays *27*, 849–857. https://doi.org/10.1002/BIES.20261.
38. Abramson, J., Adler, J., Dunger, J., Evans, R., Green, T., Pritzel, A., Ronneberger, O., Willmore, L., Ballard, A.J., Bambrick, J., et al. (2024). Accurate structure prediction of biomolecular interactions with AlphaFold 3. Nature *630*, 493–500. https://doi.org/10.1038/S41586-024-07487-W.
39. Kiefer, P., and Dickson, C. (1995). Nucleolar association of fibroblast growth factor 3 via specific sequence motifs has inhibitory effects on cell growth. Mol Cell Biol *15*, 4364–4374. https://doi.org/10.1128/MCB.15.8.4364.
40. Goetz, R., Beenken, A., Ibrahimi, O.A., Kalinina, J., Olsen, S.K., Eliseenkova, A. V., Xu, C., Neubert, T.A., Zhang, F., Linhardt, R.J., et al. (2007). Molecular insights into the klotho-dependent, endocrine mode of action of fibroblast growth factor 19 subfamily members. Mol Cell Biol *27*, 3417–3428. https://doi.org/10.1128/MCB.02249-06.
41. Wu, X., and Li, Y. (2012). Understanding the structure-function relationship between FGF19 and its mitogenic and metabolic activities. Adv Exp Med Biol *728*, 195–213. https://doi.org/10.1007/978-1-4614-0887-1_13.
42. Foletti, A., Vuadens, F., and Beermann, F. (2003). Nuclear localization of mouse fibroblast growth factor 2 requires N-terminal and C-terminal sequences. Cell Mol Life Sci *60*, 2254–2265. https://doi.org/10.1007/S00018-003-3258-6.
43. Beenken, A., and Mohammadi, M. (2009). The FGF family: biology, pathophysiology and therapy. Nat Rev Drug Discov *8*, 235–253. https://doi.org/10.1038/NRD2792.
44. Więdłocha, A., and Sørensen, V. (2004). Signaling, internalization, and intracellular activity of fibroblast growth factor. Curr Top Microbiol Immunol *286*, 45–79. https://doi.org/10.1007/978-3-540-69494-6_3.
45. Kiefer, P., Strähle, U., and Dickson, C. (1996). The zebrafish Fgf-3 gene: CDNA sequence, transcript structure and genomic organization. Gene *168*, 211–215. https://doi.org/10.1016/0378-1119(95)00736-9.
46. Shin, Y.J., Park, S.K., Jung, Y.J., Kim, Y.N., Kim, K.S., Park, O.K., Kwon, S.H., Jeon, S.H., Trinh, L.A., Fraser, S.E., et al. (2015). Nanobody-targeted E3-ubiquitin ligase complex degrades nuclear proteins. Sci Rep *5*, 14269. https://doi.org/10.1038/srep14269.
47. Ebeid, M., and Huh, S.H. (2017). FGF signaling: diverse roles during cochlear development. BMB Rep *50*, 487–495. https://doi.org/10.5483/BMBREP.2017.50.10.164.
48. Gardiner, J.R., Jackson, A.L., Gordon, J., Lickert, H., Manley, N.R., and Albert Basson, M. (2012). Localised inhibition of FGF signalling in the third pharyngeal pouch is required for normal thymus and parathyroid organogenesis. Development *139*, 3456–3466. https://doi.org/10.1242/DEV.079400.

49. Alshoubaki, Y.K., Lu, Y.-Z., Legrand, J.M.D., Karami, R., Fossat, M., Salimova, E., Julier, Z., and Martino, M.M. (2023). A superior extracellular matrix binding motif to enhance the regenerative activity and safety of therapeutic proteins. NPJ Regen Med *8*, 25. https://doi.org/10.1038/s41536-023-00297-0.
50. Xie, Y., Su, N., Yang, J., Tan, Q., Huang, S., Jin, M., Ni, Z., Zhang, B., Zhang, D., Luo, F., et al. (2020). FGF/FGFR signaling in health and disease. Signal Transduct Target Ther *5*. https://doi.org/10.1038/S41392-020-00222-7.
51. Mikolajczak, M., Goodman, T., and Hajihosseini, M.K. (2016). Interrogation of a lacrimo-auriculo-dento-digital syndrome protein reveals novel modes of fibroblast growth factor 10 (FGF10) function. Biochem J *473*, 4593–4607. https://doi.org/10.1042/BCJ20160441.
52. Di Tommaso, P., Moretti, S., Xenarios, I., Orobitg, M., Montanyola, A., Chang, J.M., Taly, J.F., and Notredame, C. (2011). T-Coffee: a web server for the multiple sequence alignment of protein and RNA sequences using structural information and homology extension. Nucleic Acids Res *39*. https://doi.org/10.1093/NAR/GKR245.
53. Robert, X., and Gouet, P. (2014). Deciphering key features in protein structures with the new ENDscript server. Nucleic Acids Res *42*. https://doi.org/10.1093/NAR/GKU316.
54. Westerfield, M. (2007). The Zebrafish Book; A guide for the laboratory use of zebrafish (Danio rerio). Univ. Oregon Press.
55. Distel, M., Wullimann, M.F., and Köster, R.W. (2009). Optimized Gal4 genetics for permanent gene expression mapping in zebrafish. Proc Natl Acad Sci U S A *106*, 13365–13370. https://doi.org/10.1073/PNAS.0903060106.
56. Wada, H., Ghysen, A., Satou, C., Higashijima, S. ichi, Kawakami, K., Hamaguchi, S., and Sakaizumi, M. (2010). Dermal morphogenesis controls lateral line patterning during postembryonic development of teleost fish. Dev Biol *340*, 583–594. https://doi.org/10.1016/J.YDBIO.2010.02.017.
57. Kwan, K.M., Fujimoto, E., Grabher, C., Mangum, B.D., Hardy, M.E., Campbell, D.S., Parant, J.M., Yost, H.J., Kanki, J.P., and Chien, C. Bin (2007). The Tol2kit: a multisite gateway-based construction kit for Tol2 transposon transgenesis constructs. Dev Dyn *236*, 3088–3099. https://doi.org/10.1002/DVDY.21343.
58. Marques, S.R., Lee, Y., Poss, K.D., and Yelon, D. (2008). Reiterative roles for FGF signaling in the establishment of size and proportion of the zebrafish heart. Dev Biol *321*, 397–406. https://doi.org/10.1016/J.YDBIO.2008.06.033.
59. Rapsomaniki, M.A., Kotsantis, P., Symeonidou, I.E., Giakoumakis, N.N., Taraviras, S., and Lygerou, Z. (2012). easyFRAP: an interactive, easy-to-use tool for qualitative and quantitative analysis of FRAP data. Bioinformatics *28*, 1800–1801. https://doi.org/10.1093/BIOINFORMATICS/BTS241.
60. Irizarry, R.A., Hobbs, B., Collin, F., Beazer-Barclay, Y.D., Antonellis, K.J., Scherf, U., and Speed, T.P. (2003). Exploration, normalization, and summaries of high density oligonucleotide array probe level data. Biostatistics *4*, 249–264. https://doi.org/10.1093/BIOSTATISTICS/4.2.249.
61. Lockstone, H.E. (2011). Exon array data analysis using Affymetrix power tools and R statistical software. Brief Bioinform *12*, 634–644. https://doi.org/10.1093/BIB/BBQ086.
62. Lockstone, H.E. (2011). Exon array data analysis using Affymetrix power tools and R statistical software. Brief Bioinform *12*, 634–644. https://doi.org/10.1093/BIB/BBQ086.
63. Mackmull, M.T., Iskar, M., Parca, L., Singer, S., Bork, P., Ori, A., and Beck, M. (2015). Histone Deacetylase Inhibitors (HDACi) Cause the Selective Depletion of

Bromodomain Containing Proteins (BCPs). Mol Cell Proteomics *14*, 1350–1360. https://doi.org/10.1074/MCP.M114.042499.
64. Ritchie, M.E., Phipson, B., Wu, D., Hu, Y., Law, C.W., Shi, W., and Smyth, G.K. (2015). limma powers differential expression analyses for RNA-sequencing and microarray studies. Nucleic Acids Res *43*, e47. https://doi.org/10.1093/NAR/GKV007.
65. Gentleman, R.C., Carey, V.J., Bates, D.M., Bolstad, B., Dettling, M., Dudoit, S., Ellis, B., Gautier, L., Ge, Y., Gentry, J., et al. (2004). Bioconductor: open software development for computational biology and bioinformatics. SpringerPaperpileRC Gentleman, VJ Carey, DM Bates, B Bolstad, M Dettling, S Dudoit, B Ellis, L Gautier, Y GeGenome biology, 2004•SpringerSign in *5*.
66. Benjamini, Y., and Hochberg, Y. (1995). Controlling the False Discovery Rate: A Practical and Powerful Approach to Multiple Testing. J R Stat Soc Series B Stat Methodol *57*. https://doi.org/10.1111/j.2517-6161.1995.tb02031.x.
67. Letunic, I., Khedkar, S., and Bork, P. (2021). SMART: Recent updates, new developments and status in 2020. Nucleic Acids Res *49*, D458–D460. https://doi.org/10.1093/NAR/GKAA937,.
68. Abramson, J., Adler, J., Dunger, J., Evans, R., Green, T., Pritzel, A., Ronneberger, O., Willmore, L., Ballard, A.J., Bambrick, J., et al. (2024). Accurate structure prediction of biomolecular interactions with AlphaFold 3. Nature *630*, 493–500. https://doi.org/10.1038/S41586-024-07487-W.
69. Jurrus, E., Engel, D., Star, K., Monson, K., Brandi, J., Felberg, L.E., Brookes, D.H., Wilson, L., Chen, J., Liles, K., et al. (2018). Improvements to the APBS biomolecular solvation software suite. Protein Science *27*, 112–128. https://doi.org/10.1002/PRO.3280,.
70. Dolinsky, T.J., Czodrowski, P., Li, H., Nielsen, J.E., Jensen, J.H., Klebe, G., and Baker, N.A. (2007). PDB2PQR: Expanding and upgrading automated preparation of biomolecular structures for molecular simulations. Nucleic Acids Res *35*. https://doi.org/10.1093/NAR/GKM276,.
71. Lunin, V.Y., Urzhumtsev, A., Bockmayr, A., Fokin, A., Urzhumtsev, A., Afonine, P., Lunin, V.Y., Harding, M., Turkenburg, M., Ballard, C., et al. Pymol: An open-source molecular graphics tool. CiteseerWL DeLanoCCP4 Newsl. Protein Crystallogr, 2002•Citeseer.
72. Lange, A., Mills, R.E., Lange, C.J., Stewart, M., Devine, S.E., and Corbett, A.H. (2007). Classical Nuclear Localization Signals: Definition, Function, and Interaction with Importin α. Journal of Biological Chemistry *282*, 5101–5105. https://doi.org/10.1074/jbc.R600026200.
73. R Core Team. (2023). R: A language and environment for statistical computing. R Foundation for Statistical Computing, Vienna, Austria. Open J Stat *13*.
74. Wickham, H. (2016). ggplot2: Elegant Graphics for Data Analysis (Springer-Verlag New York).